THE OBSERVATORIES

OF THE CARNEGIE INSTITUTION OF WASHINGTON

Magellan 2 Primary Mirror
Final Reports

01PR0004 Final Polishing Report

4/30/01

01PR0005 Dig/scratch Report

6/14/01

01PR0006 Scope of Work Compliance

6/22/01

01PR0007 Integration Report

6/27/01

813 SANTA BARBARA STREET - PASADENA - CALIFORNIA 91101

TELEPHONE (626) 577-1122 FAX (626) 795-8136

1. Project summary

The second Magellan primary mirror was cast, generated and polished by the Steward Observatory Mirror Lab during the period Month 1998 - March 2001. The casting procedure is described by Olbert *et al.*[1] Generating and polishing procedures were similar to those used for the MMT primary mirror[2] and the first Magellan primary mirror.[3] This report documents the quality of the finished mirror in terms of mechanical geometry, surface finish, figure accuracy and inferred image quality.

The mirror promises excellent performance. The structure is sound and has the superb mechanical and thermal characteristics of the honeycomb sandwich. The mirror is diffraction-limited (Strehl ratio = 0.79) at λ = 500 nm, and focuses 80% of the light into a diameter of 0.08″.

The procedures used for generating, loose-abrasive grinding and polishing of the rear surface, and loose-abrasive grinding of the front surface were essentially identical to those used for the first Magellan mirror.[3] Measurements during loose-abrasive grinding and the early polishing stages were made with the same 10.6 micron interferometer and null lens used for the first mirror.

We polished the front surface using, at different times, laps with bare pitch and thin plastic pads on pitch. We used bare pitch with rouge as the polishing compound for the final several months, since this combination gave the best surface finish (microroughness).

We made the first measurements at visible wavelength in August 2000. We used a new Twyman-Green interferometer with a 633 nm helium-neon laser (described in Section 4.1) for all visible measurements. This interferometer eliminated some problems associated with wavelength instability in the original Fizeau interferometer with its 531 nm frequency-doubled YAG laser. The null lens used for the first mirror was re-spaced to account for the change in laser wavelength, and its accuracy was verified with a new computer-generated hologram designed for the new wavelength. The mirror was figured to match a template defined by this hologram.

We used the stressed lap to remove both axisymmetric and asymmetric large-scale figure errors and to obtain passive smoothing on scales less than about 20 cm. We also ran axisymmetric strokes with passive laps of 8-25 cm diameter to remove narrow high zones, and performed asymmetric manual polishing with passive laps of 8-15 cm diameter to reduce irregular small-scale structure. We reached the final accuracy in March 2000.

Shortly after the final polishing run, we realized that the measurements contained high-spatial-frequency noise due to scattered light in the interferometer, and that the mirror figure was significantly better on scales of 1-2 pixels than the measurements had indicated. The effect was greatest for subaperture measurements made with twice the spatial resolution as the full-aperture measurements. We then covered some metal surfaces in the interferometer with absorbing material and cleaned the optics, reducing the noise by a factor of 2. The final subaperture measurements shown in Section 5.3 are still somewhat limited by interferometer noise, and we have quantified the effect and made a correction for it. We present the data with and without this correction.

2. Specifications

2.1 Prescription

The optical prescription is a paraboloid. For purposes of tolerance analysis, we treat it as a conic section defined by the radius of curvature R and conic constant k. The surface height z as a function of distance r from the axis of symmetry is

$$z(r) = \frac{r^2}{R + \sqrt{R^2 - (k+1)r^2}}. \tag{1}$$

The values and tolerances of the radius of curvature and conic constant are given by the Technical Specifications and Requirements[4]:

$$R = 16256 \pm 3 \text{ mm}, \tag{2}$$

$$k = -1.0000 \pm 0.0002, \tag{3}$$

and the errors in R and k must satisfy

$$\left|\Delta R + (3.2\times10^5 \text{mm})\Delta k\right| < 40 \text{ mm}. \tag{4}$$

The last condition constrains the conic error to roughly ± 0.00012.

2.2 Figure error

The figure specification is given by a wavefront structure function $\delta^2(r)$, the mean square wavefront difference between points in the aperture as a function of separation r. It is the structure function produced by the standard model of atmospheric seeing, with two modifications. The standard atmospheric structure function is

$$\delta^2 = \left(\frac{\lambda}{2\pi}\right)^2 6.88\left(\frac{r}{r_0}\right)^{5/3}, \tag{5}$$

where r_0 is the Fried parameter, related to image FWHM θ as

$$\theta = 0.980\left(\frac{\lambda}{r_0}\right). \tag{6}$$

The first modification tightens the specification at large separations by removing that part of the atmospheric structure function corresponding to mean wavefront tilt. (This is done because autoguiding will remove mean tilt, or image motion, in the telescope, and the laboratory figure measurements are insensitive to it.) Hufnagel[5] gives an approximate expression for this correction, which depends only on telescope diameter D. The second modification is a relaxation at small separations corresponding to scattering a fraction L of the light outside of the seeing disk. The scattering loss is related to the small-scale rms phase error σ as

$$L = 1 - e^{-\sigma^2}. \tag{7}$$

The full specification is then

$$\delta^2 = \left(\frac{\lambda}{2\pi}\right)^2 \left\{ 6.88 \left(\frac{r}{r_0}\right)^{5/3} \left[1 - 0.975 \left(\frac{r}{D}\right)^{1/3} \right] + 2\sigma^2 \right\}. \tag{8}$$

The two parameters that fix its amplitude are

$$r_0 = 1.18 \text{ m}, \tag{9}$$

$$L = 0.015, \tag{10}$$

both defined at $\lambda = 500$ nm. This specification is plotted along with the measured structure functions in Figures 7 and 12.

2.3 Clear aperture

The clear aperture is defined as the annular region with

$$\text{ID} = 923 \text{ mm}, \tag{11}$$

$$\text{OD} = 6478 \text{ mm}. \tag{12}$$

The structure function is evaluated over this clear aperture, which extends to within about 11 mm of each edge of the polished surface.

2.4 Mechanical dimensions

Mechanical dimensions are given by drawing 1168, Rev. C. The following tolerances are listed in the Technical Specifications and Requirements[4].

1. centration of optical axis with respect to mechanical center: 1 mm
2. vertex thickness: 385.1 ± 0.5 mm
3. wedge angle: 30″

2.5 Micro-roughness

The polished surface must have a roughness less than 20 Angstroms on scales << 1 cm.

2.6 Scratches, digs and bubbles

Limits on the numbers and sizes of scratches, digs and bubbles in the optical surface are listed in the Technical Specifications and Requirements[4].

3. Conventions and notation

3.1 Orientation of coordinates

All figure maps show the optical surface as viewed face-on with the mirror horizon-pointing. Rotation angles quoted throughout this report use the same view. The x and y axes are in the usual sense, x increasing to the right and y increasing upward. Angles increase counter-clockwise from 0 in the positive x direction. This convention holds for descriptions of the back plate as well as the optical surface, i. e. one views the back plate through the mirror.

3.2 Zernike polynomial coefficients

We use Zernike polynomial coefficients to describe the aberrations of focus, astigmatism, coma and spherical aberration. Throughout this report, amplitudes of these aberrations are given in terms of the Zernike coefficient of surface error. The symbols used for coefficients and the associated polynomials are given in Table 1. Some of the symbols are different than those used in Reference 3, as those conflict with established usage. The polynomials are expressed as functions of the dimensionless radius ρ normalized to 1 at the edge of the mirror.

Table 1. Zernike polynomial coefficients

aberration	coefficient	polynomial
focus	F	$2\rho^2 - 1$
astigmatism (0°)	A_0	$\rho^2 \cos(2\theta)$
astigmatism (45°)	A_{45}	$\rho^2 \sin(2\theta)$
coma (0°)	C_0	$(3\rho^3 - 2\rho)\cos\theta$
coma (90°)	C_{90}	$(3\rho^3 - 2\rho)\sin\theta$
spherical aberration	S	$6\rho^4 - 6\rho^2 + 1$

We sometimes describe astigmatism by the combined Zernike coefficient

$$A = [(A_0)^2 + (A_{45})^2]^{1/2} \tag{13}$$

and the rotation angle

$$\theta_a = \frac{1}{2}\text{atan}\left(\frac{A_{45}}{A_0}\right) \tag{14}$$

at which the high occurs.

Spherical aberration is equivalent to a change in conic constant; the relation between Zernike coefficient S and conic change Δk is

$$\Delta k = 6144 f^3 \frac{S}{D}, \tag{15}$$

where $f = 1.25$ is the focal ratio and $D = 6.5$ m is the diameter. If Δk is expressed in parts per million,

$$\frac{\Delta k}{1 \text{ ppm}} = 1.846\left(\frac{S}{1 \text{ nm}}\right). \tag{16}$$

Positive spherical aberration corresponds to a less negative conic constant.

3.3 Uncertainties

All uncertainties quoted in this report represent our best estimate of two standard deviations. In other words, a value quoted as $x \pm \Delta x$ means that we estimate that the value lies within that range with 95% probability. This interpretation is valid only for anticipated sources of error.

4. Procedure for figure measurements and analysis

4.1 Measurement system

Optical tests were performed from the center of curvature with the mirror mounted on its polishing support cell. The measurement system comprises a Twyman-Green interferometer with a helium-neon laser at 633 nm, a pair of lenses that image the mirror onto a CCD camera, and an Offner-type refractive null corrector. Two separate sets of imaging optics are used; one images the full mirror onto the CCD while the other magnifies the image by a factor of 2 and is used for subaperture measurements.

The measurement is made by phase-shifting interferometry, in which the phase variations across the pupil are determined from a series of intensity patterns with phase shifts between them. The interferometer's flat reference mirror is translated with piezoelectric transducers to introduce a phase shift, constant across the pupil, between successive intensity patterns. Intensity patterns are recorded at a 110 Hz frame rate, and reduced to phase measurements using a commercial system from Diffraction International. The CCD camera has square pixels and a resolution of 232 pixels across the mirror in the full-aperture measurement. This gives a pixel spacing of 28 mm and represents an 18% improvement in resolution over the full-aperture measurements of the first Magellan mirror.

4.2 Measurement noise

Any single phase map contains random errors due to local air turbulence and vibration. They are reduced by taking many phase maps and averaging. The error in an individual full-aperture map, computed as the difference between that map and the average of all maps, is in the range 20-30 nm rms surface error after subtracting astigmatism. These errors average out as random noise, with the possible exception of large-scale features which may persist for 10 s or more and therefore correlate among two or more maps. Both full-aperture and subaperture maps presented here are averages of 40 individual maps. We estimate that the contribution of turbulence and vibration in the average map is less than 5 nm rms surface error, ignoring astigmatism. The contribution to the structure function at the critical 5-10 cm separations is not significant.

We discovered near the end of the process that the interferometer was contributing a substantial amount of noise on small scales, especially to the subaperture measurements. We investigated this noise by measuring the small reference sphere (glass ball) that can be inserted at the focus formed by the interferometer, between the interferometer and the null lens. This ball is normally used to measure the nominally spherical wavefront produced by the interferometer and to provide a mechanical reference for aligning the null lens to the interferometer. We measured the ball using both imaging systems, taking an average over many ball positions in order to eliminate small errors in the surface of the ball. The initial measurements showed structure of roughly 7 nm rms surface error with little correlation between adjacent pixels but strong correlation between separate measurements. In addition there were many sets of small diffraction rings apparently due to dust on optical surfaces. The net effect was that the measurements of the ball did not meet the primary mirror specification using the 2X imaging system.

We noticed that laser light was scattering off of several metal surfaces in the interferometer, so we added flocking paper (black felt paper) to these surfaces. We also cleaned the lenses, mirrors and beamsplitter in the interferometer. After several iterations, the noise was reduced by a factor of 2. Figures 1 and 2 show the measurements of the ball taken after the improvements to the interferometer. These are averages of 40 individual maps, with the ball rotated between measurements. Figure 3 shows the structure functions, measured over the same image coordinates used for the corresponding measurements of the primary mirror. The noise is now significant only in the 2X imaging system. This is partly because a 1-pixel separation corresponds to a smaller separation on the primary, where the specification is tighter, but also because the noise is higher in that imaging system.

In Section 5 we present the structure functions of the primary mirror measurements, with and without a correction for the interferometer noise. For the corrected data, we subtract the structure function (defined as mean square wavefront difference) of the ball from that of the primary mirror. All data sets are averages of 40 individual maps.

4.3 Mirror support

The mirror is supported on passive hydraulic cylinders that match the telescope support system in location and force. Differences between the support mechanisms in the polishing cell and the telescope cell are expected to cause force differences on the order of 10 N. Uncontrolled force variations in the polishing support, probably related to friction in the supports, cause significant changes in astigmatism and smaller changes in other flexible bending modes. Most of their effects will be removed through the empirical optimization of support forces in the telescope cell.

Plastic skirts used to collect polishing slurry at the inner and outer edges of the mirror were removed for all measurements reported here, so the only mechanical contact with the mirror was through the 104 supports and the 3 tangent rods that provide a kinematic constraint against translation and rotation.

4.4 Thermal equilibration

All figure measurements reported here were made about 3 weeks after the final polishing run. We relied on passive equilibration rather than ventilation to make the mirror isothermal. We did not routinely measure the temperature distribution in the mirror, but experience with the first Magellan mirror indicated that the mirror was isothermal within 0.2 K or better in these conditions.

The final figure measurements show significant amounts of certain low-order aberrations that were not present during the last few cycles of in-process measurements. These include trefoil and fifth-order astigmatism, which are relatively flexible bending modes and could change due to small changes in support forces, and fifth-order spherical aberration, a much stiffer mode that is more likely to change due to temperature gradients.

Because of air turbulence, we generally had to turn the lab's air handlers off for about 45 minutes before measuring the mirror. (For the first Magellan mirror, we were able to measure almost immediately after turning the air handlers off, and we do not understand the difference.)

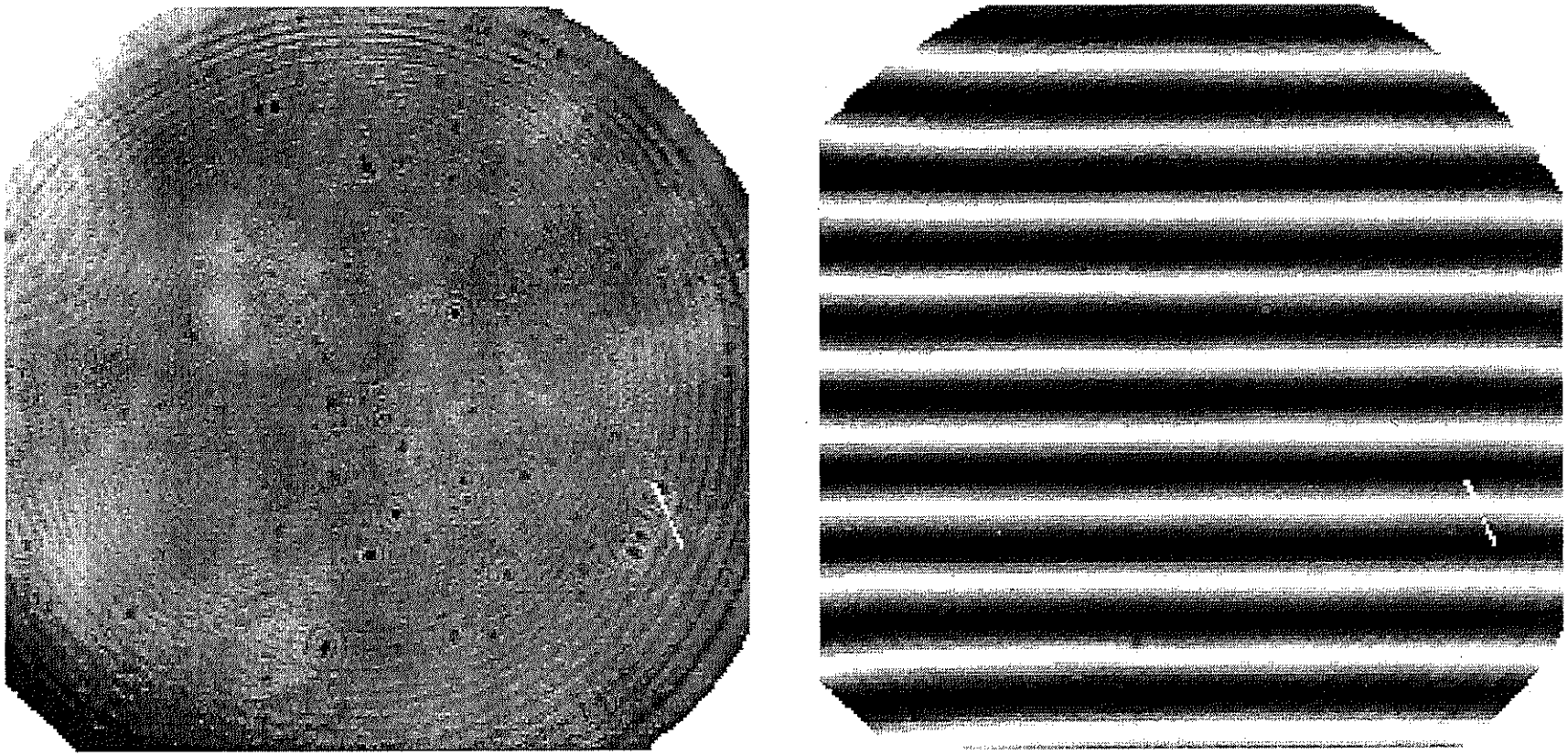

Figure 1. Gray-scale map of the surface error and synthetic interference pattern for the measurement of the interferometer's reference sphere, using the 1X imaging optics that were used for the full-aperture measurements of the primary mirror. The gray scale covers ±25 nm of surface. This is an average of 40 measurements with the ball rotated between measurements. All aberrations through fourth order in r have been subtracted. The displays have not yet been trimmed to the aperture used for measurements of the primary mirror. This aperture is a circle inscribed in the square border of the array displayed here.

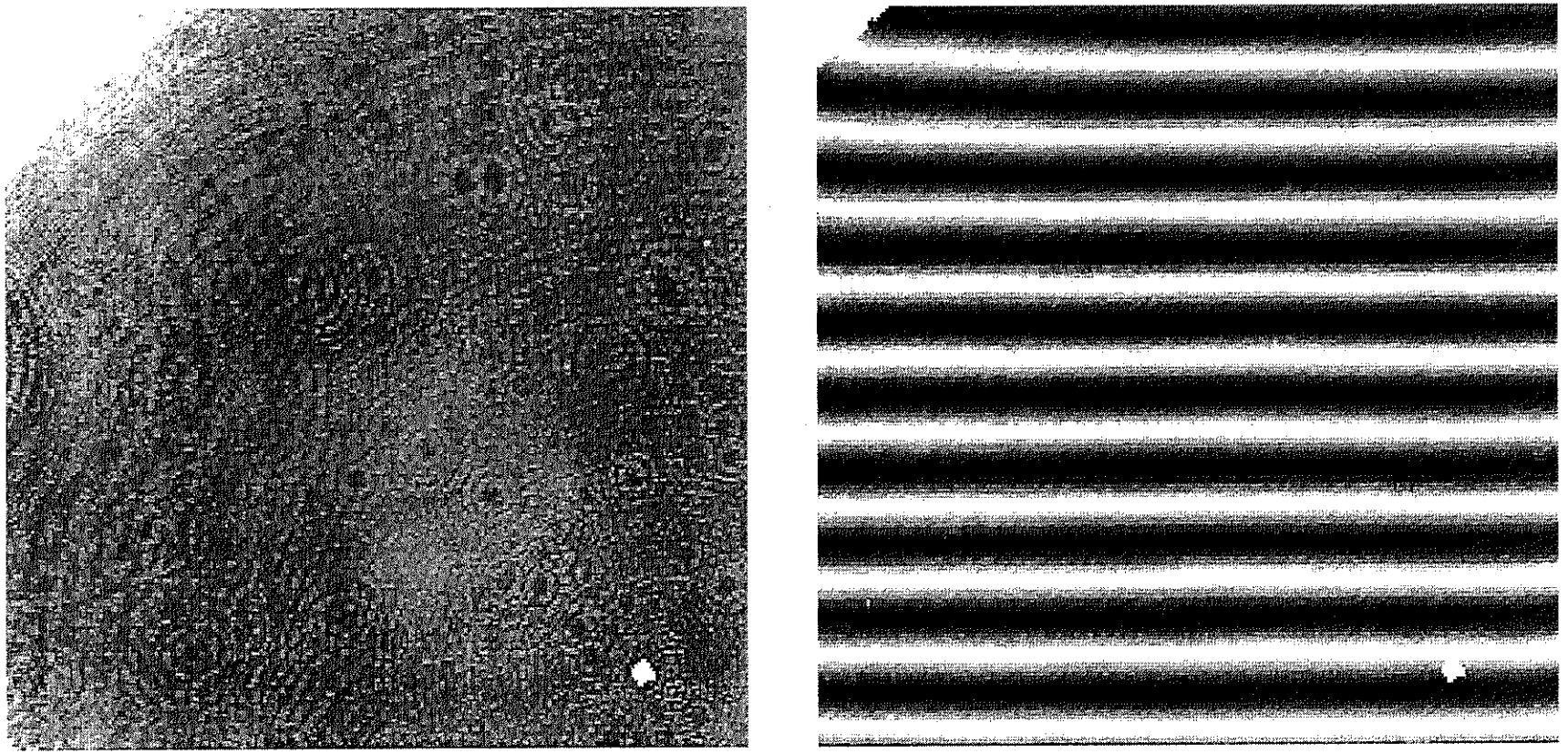

Figure 2. Gray-scale map of the surface error and synthetic interference pattern for the measurement of the interferometer's reference sphere, using the 2X imaging optics that were used for the subaperture measurements of the primary mirror. The gray scale covers ±25 nm of surface. This is an average of 40 measurements with the ball rotated between measurements. All aberrations through third order in r have been subtracted. The displays have not yet been trimmed to the aperture used for measurements of the primary mirror. This aperture is roughly the upper left quadrant of a circle centered near the lower right corner of the display and extending to the top and left borders.

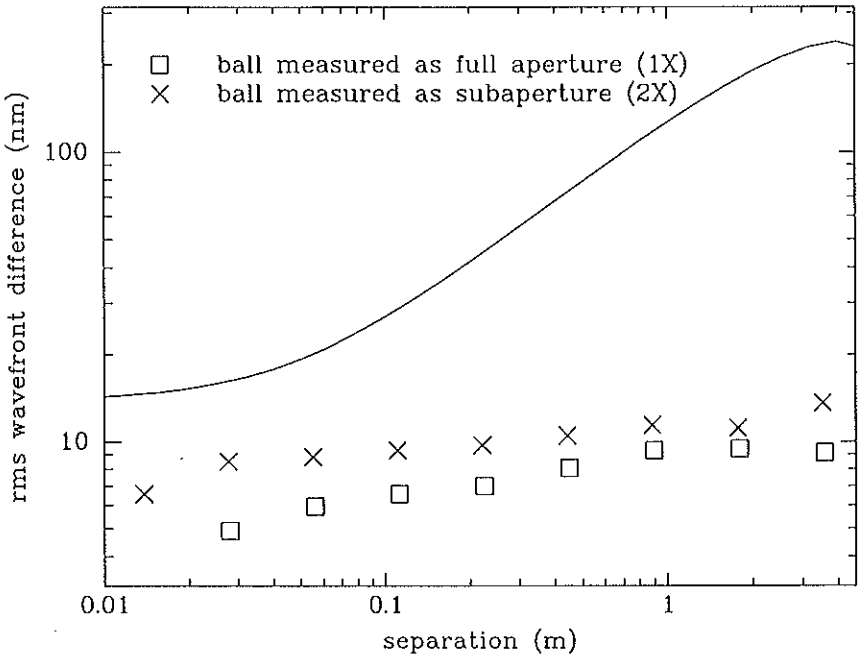

Figure 3. Square root of the wavefront structure function for the maps of the reference sphere shown in Figures 1 and 2. The measured aperture includes the same pixels used to calculate the primary mirror's structure function. The curve is the specification.

During this time the average air temperature in the vicinity of the mirror rose by about 0.1 K, and rose an additional 0.15 K during the hour or so needed to obtain 40 good maps. While this procedure was followed for all measurements during and after the last few months of polishing, one change that occurred before the final measurements is that the protective outer walls and the panels at the bottom of the cell were removed. Thus the mirror was more exposed to ambient air.

There is some evidence that the fifth-order spherical aberration increases during the time required to take 40 measurements. If so, the aberration in the data presented here overestimates the amount in an isothermal mirror. Even with this and other questionable low-order aberrations, the mirror figure clearly meets the specification. We plan to analyze the figure measurements in more detail to better estimate the figure in equilibrium.

4.5 Removal of test optics errors

We determine the errors in the test optics by measuring a computer-generated hologram that mimics the ideal primary mirror. The principles and procedure are described in Section 7.3. We subtract a Zernike polynomial representation of the hologram map from all full-aperture maps of the primary mirror. The map of the hologram contains spherical aberration $S = -35$ nm, equivalent to an error in conic constant of -70 parts per million. This is within the expected un-

certainty of the null lens. An additional spherical aberration correction is made for the small error in the primary radius of curvature as described in Section 6.4.

4.6 Treatment of tilt, defocus and coma

The test optics are mounted in a stiff frame that is positioned relative to the mirror with remotely controlled translation and rotation stages. These stages are used to align the test optics in five degrees of freedom: horizontal and vertical translations and tilt in both directions. This alignment is adjusted to minimize tilt, defocus and coma in the reflected wavefront as judged by visual inspection of the interference pattern. Residual aberrations of these forms are subtracted from the measured phase map. The aberrations of tilt, defocus and coma are constrained by measured limits on wedge, radius of curvature and centration of the optical axis, respectively. These quantities are measured separately as described in Section 6.

4.7 Treatment of astigmatism and spherical aberration

We measured varying amounts of third-order astigmatism throughout the fabrication process, including the final figure measurements. We believe the variations are related to support forces. The astigmatism varied in magnitude from about 100 to 450 nm among figure measurements made on different days after polishing was completed. These variations did not come from noise in the data, for the variations among maps measured on a given day were much smaller. We estimated the support forces necessary to cause this much astigmatism from a modal analysis of the BCV finite-element calculations.[6,7] Astigmatism with $A = 400$ nm would be caused by an optimized set of forces whose extreme values are ± 4 N, or by random force errors on the order of 14 N rms. In the telescope, astigmatism will be determined entirely by support forces rather than the relaxed mirror's figure.

Third-order spherical aberration varied by about ± 10 nm among measurements made after polishing was completed. The variation is probably caused by small temperature gradients. The final full-aperture map has less than 10 nm of third-order spherical aberration. Spherical aberration is treated as an error in conic constant rather than mirror figure.

We present full-aperture maps and structure functions with and without astigmatism and spherical aberration. The synthetic images are made from the maps with astigmatism and spherical aberration subtracted.

4.8 Distortion and measured aperture

The mapping from mirror to image is determined by placing fiducial markers at known locations on the mirror surface, and measuring their locations in the image. The conversion from image coordinates to object (mirror) coordinates is modeled as a polynomial in x and y. We fit polynomials through fourth order in x and y (third order for the subaperture maps) to the measured image coordinates and known object coordinates.

The fiducials are small annular markers at 42 positions roughly equally spaced over the mirror. Twelve of these appear in each subaperture quadrant. We used a large number of fiducials

because there is a significant distortion in the image, causing parts of it to be shifted by as much as 130 mm relative to an undistorted image. Distortion has been corrected in the maps displayed in Section 5. The structure functions are calculated using only data in the clear aperture.

4.9 Subaperture measurements

We measured four quadrants at twice the resolution of the full-aperture maps. For off-axis subaperture measurements, we cannot distinguish between alignment errors (tilt, focus and coma) and other low-order aberrations such as astigmatism and trefoil. We therefore subtract tilt, focus, coma, astigmatism and trefoil from each subaperture map. We do not subtract the map of the hologram to correct for errors in the interferometer and null lens. This may cause an incomplete removal of test-optic errors and/or an artificial reduction in large-scale aberrations, but it should have virtually no effect on the structure function at separations below about 10 cm.

4.10 Calculation of structure function

The wavefront structure function is defined as the mean square difference in wavefront error between randomly selected points as a function of their separation in the aperture. For comparison with the specification, we plot the square root of this quantity, the rms wavefront difference, along with the corresponding curve for the specification.

We compute the rms wavefront difference for discrete separations. Each point on the plot represents a bin of separation values. The bins are centered at separations of 1, 2, 4, 8, 16, 32, 64 and 128 pixels, and the bin width is 0.5 pixel. Each point on the plot gives the rms wavefront error over pairs of pixels whose separation lies in the corresponding bin.

The structure function calculation uses only discrete pixel values. There is no interpolation of values at fractional pixel coordinates. We first throw out all pixels that lie outside the clear aperture. In order to determine whether a pixel lies in the clear aperture, we convert its image coordinates to object coordinates using the mapping function determined from the fiducials. We then select a 50×50 square grid of pixels over the image. These form the set of first points of pairs used to calculate the rms difference. For each separation bin, and for each first point, we find all the pixels whose separation from the first point lies in the separation bin. We compute the rms wavefront difference over all pairs selected in this way.

5. Figure measurements

5.1 Full-aperture maps and structure functions

Figures 4-6 are gray-scale contour maps and synthetic interference patterns made from the full-aperture measurements. All measurements have been corrected for errors in the null lens as determined by the hologram, and for image distortion as determined by the fiducials. The three cases are: the original map including third-order astigmatism and spherical aberration; the map with third-order astigmatism and spherical subtracted; and the map with an additional 3 aberrations corresponding to flexible bending modes (trefoil, quatrefoil and fifth-order astigmatism) subtracted. Third-order spherical aberration is negligible. The interference patterns are calculated for a wavelength of 633 nm and contain 10 waves of tilt. Table 2 gives statistics of the maps. Figure 7 shows the wavefront structure function, calculated over the clear aperture, for all three cases.

Table 2. Statistics of full-aperture maps

map	rms surface error	A	θ_a	S
original	150 nm	370 nm	−64°	−3 nm
astigmatism and spherical aberration subtracted	20 nm			
additional 3 flexible modes subtracted	16 nm			

5.2 Synthetic images

We calculated synthetic images from the map of Figure 5, with astigmatism and spherical aberration subtracted, using the clear aperture. The calculation covers a 3.6 arcsecond field, using the full-aperture map with 232 pixels across the mirror. Figure 8 shows the point-spread functions of the actual and perfect mirrors. Figure 9 shows encircled energy diagrams for the actual mirror and a perfect mirror, in perfect seeing and 0.25 arcsecond seeing. Seeing is included by convolving the mirror's PSF with that of the seeing, calculated from its structure function.

5.3 Subaperture maps and structure functions

Figures 10 and 11 show the subaperture maps obtained with 14 mm pixels, twice the resolution of the full-aperture map. Focus, coma, astigmatism, spherical aberration and trefoil have been subtracted. Table 3 gives the rms surface errors, and Figure 12 shows the structure functions.

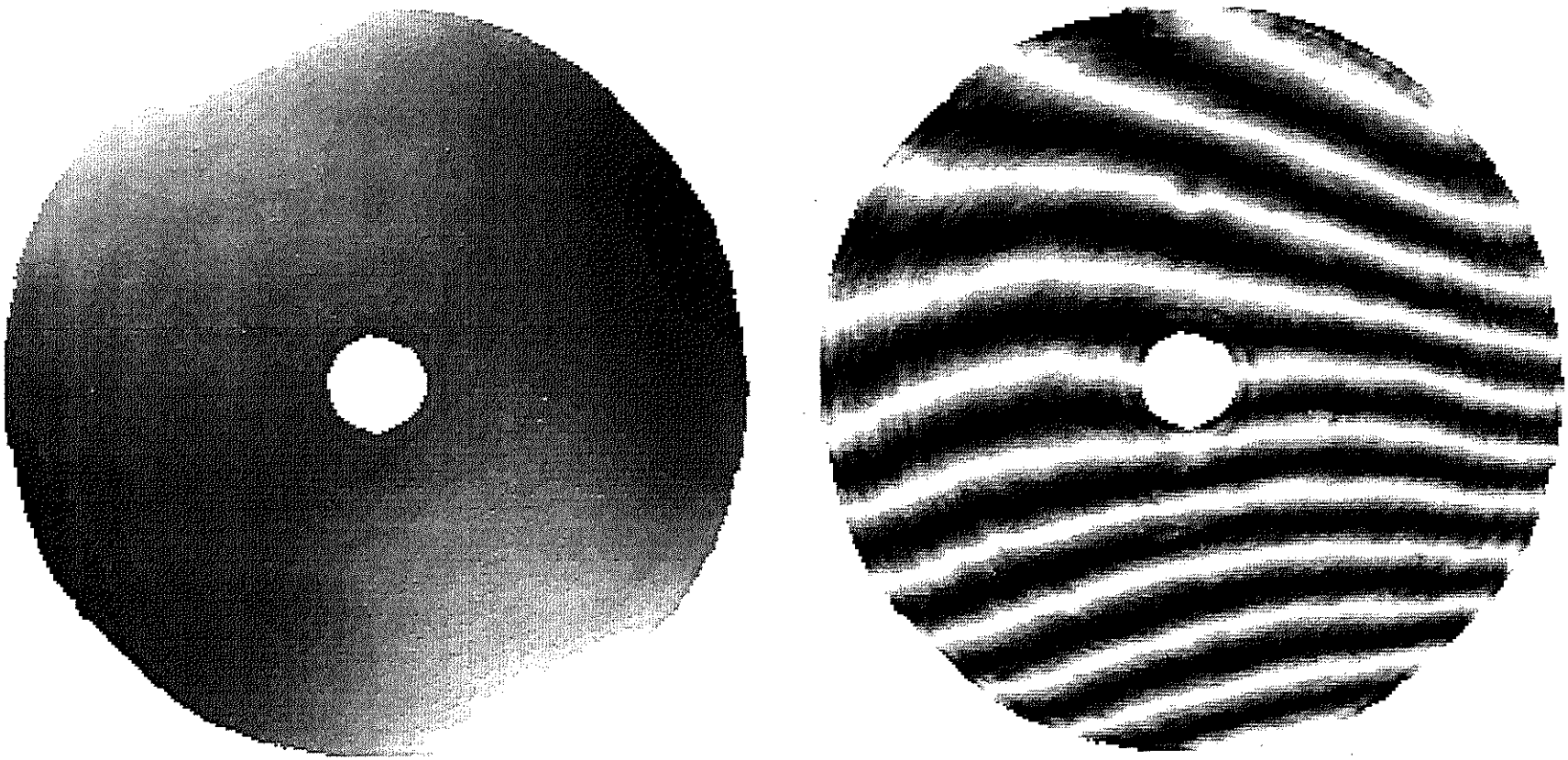

Figure 4. Gray-scale map of the mirror surface and synthetic interference pattern for the original map including astigmatism and spherical aberration. The gray scale covers ±350 nm of surface. The displays show the full measured wavefront and include some spurious pixels outside the polished surface.

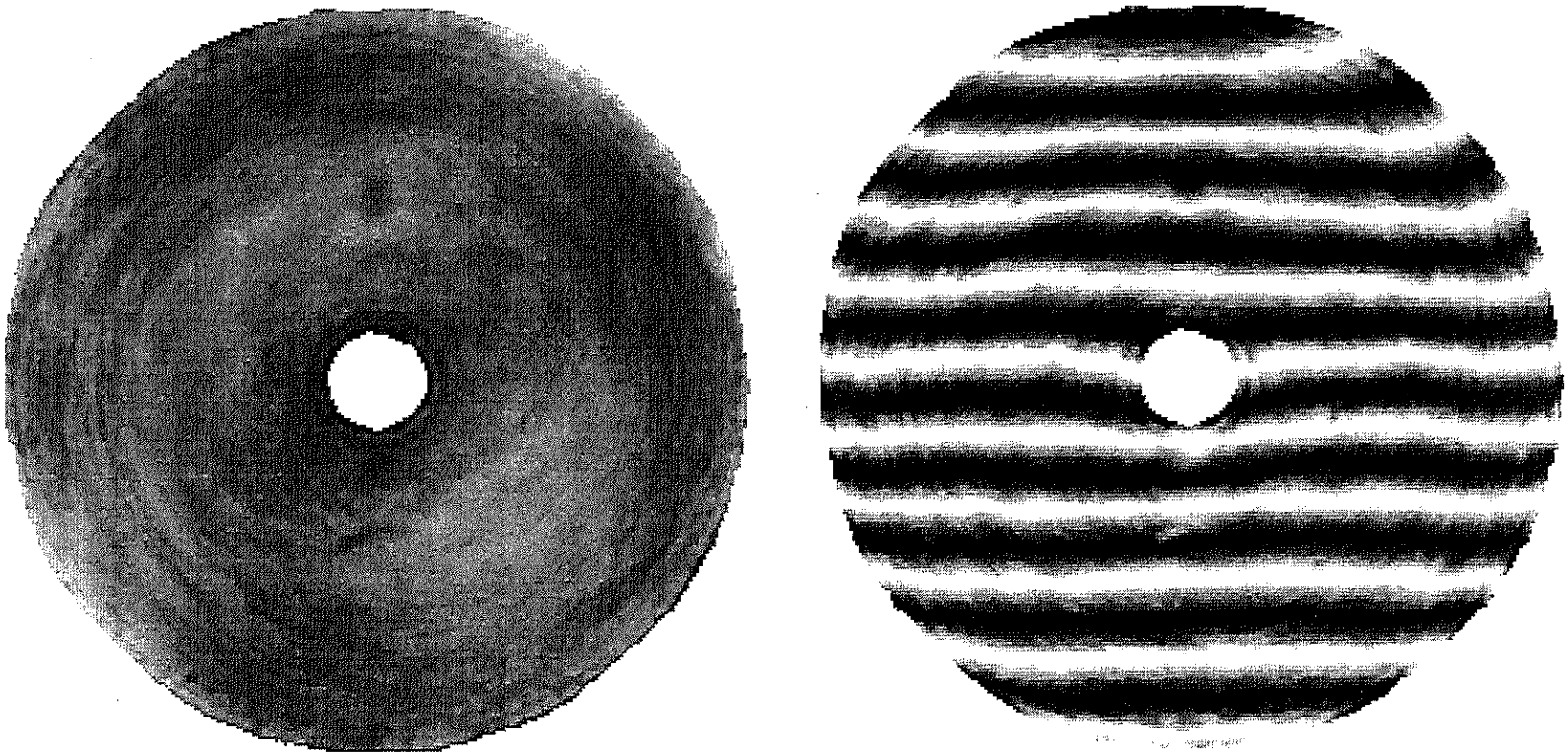

Figure 5. Gray-scale map of the mirror surface and synthetic interference pattern with astigmatism and spherical aberration subtracted. The gray scale covers ±100 nm of surface.

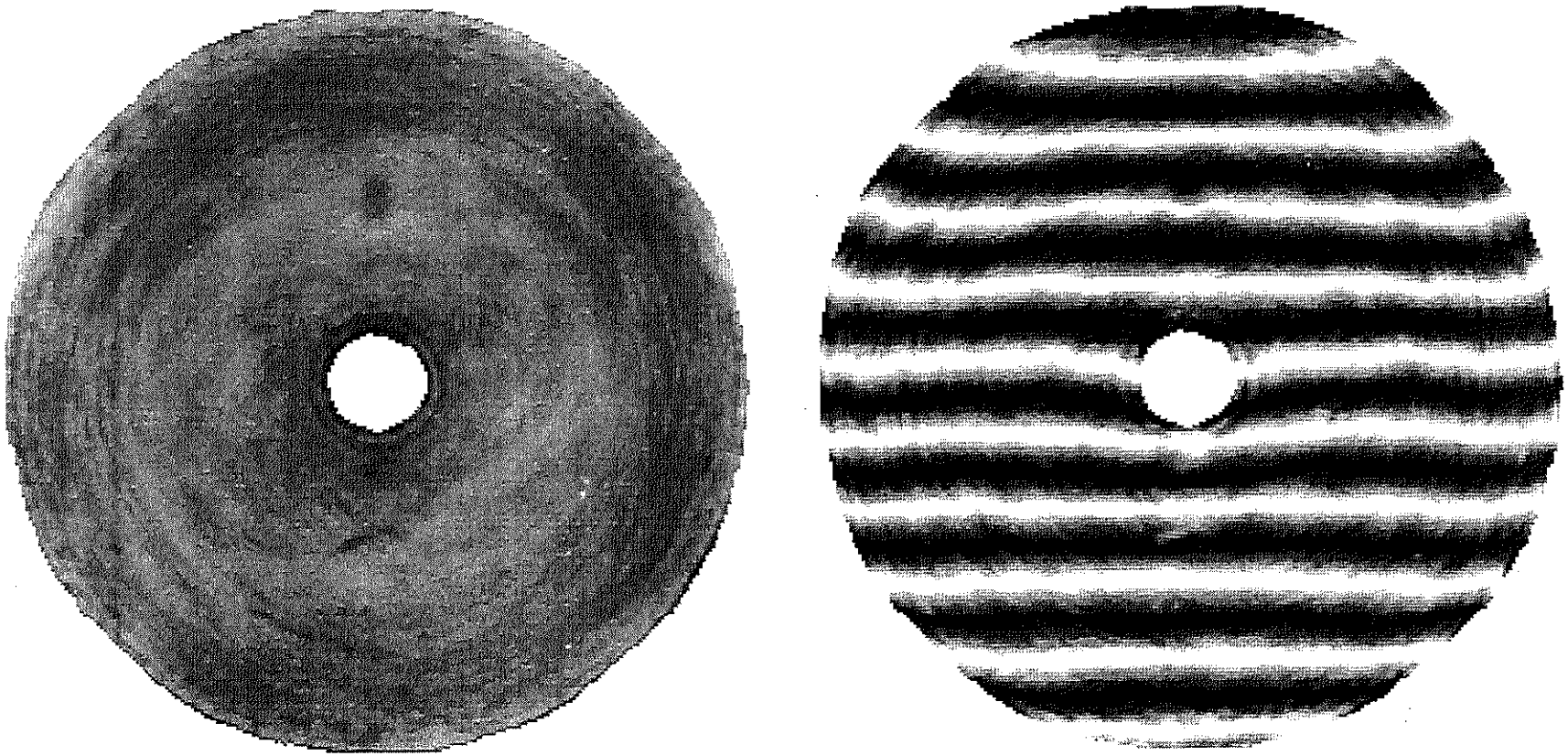

Figure 6. Gray-scale map of the mirror surface and synthetic interference pattern with astigmatism, spherical aberration, and an additional 3 flexible bending modes (trefoil, quatrefoil and fifth-order astigmatism) subtracted. The gray scale covers ±100 nm of surface.

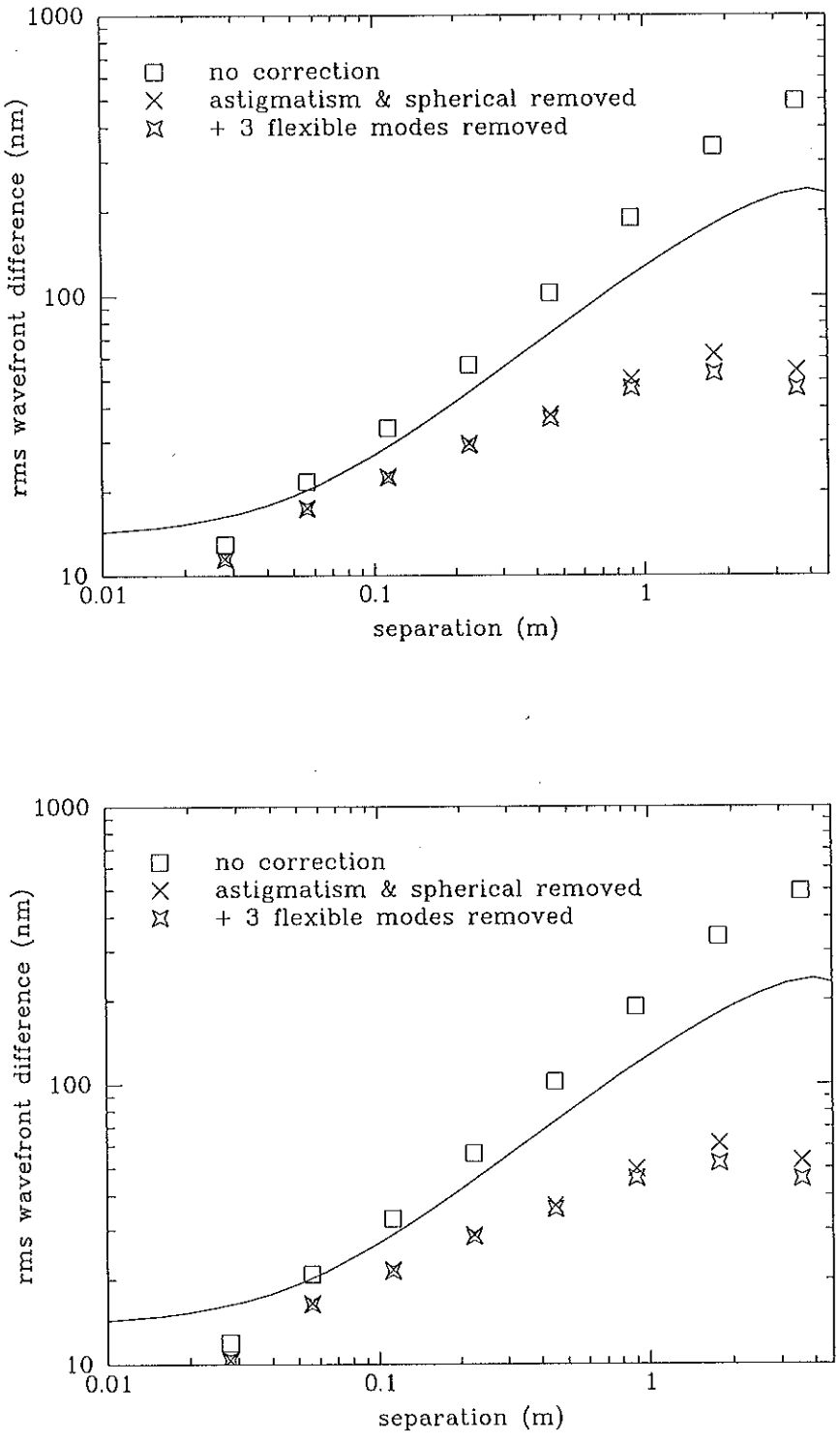

Figure 7. Square root of the wavefront structure function for the maps shown in Figures 4-6. Top: no correction for interferometer noise. Bottom: with structure function for interferometer noise subtracted. The curve is the specification.

Figure 8. Synthetic images at 0.5 micron for the actual mirror of Figure 5 (left) and a perfect mirror (right). The images are separated by 0.5 arcsecond.

Table 3. Statistics of subaperture maps

quadrant	rms surface error
1	13 nm
2	11 nm
3	11 nm
4	12 nm

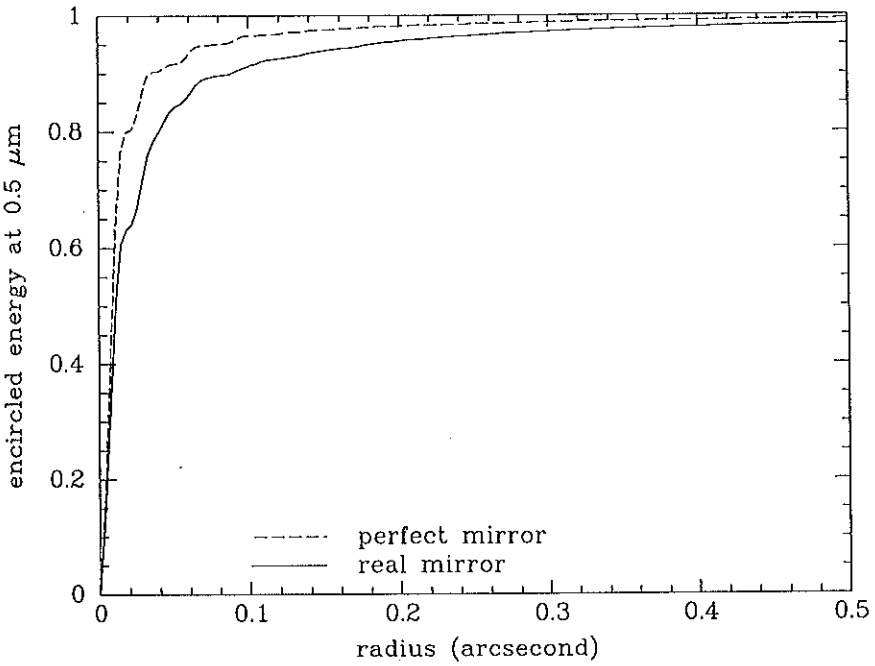

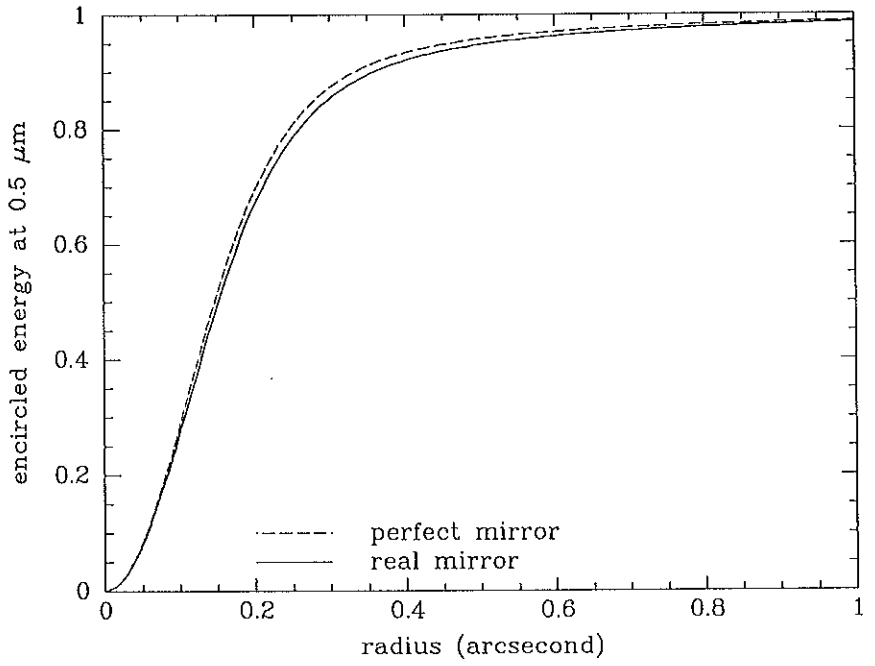

Figure 9. Encircled energy diagram with no seeing for the mirror of Figure 5 and a perfect mirror. Top: in perfect seeing. Bottom: in 0.25 arcsecond (FWHM) seeing.

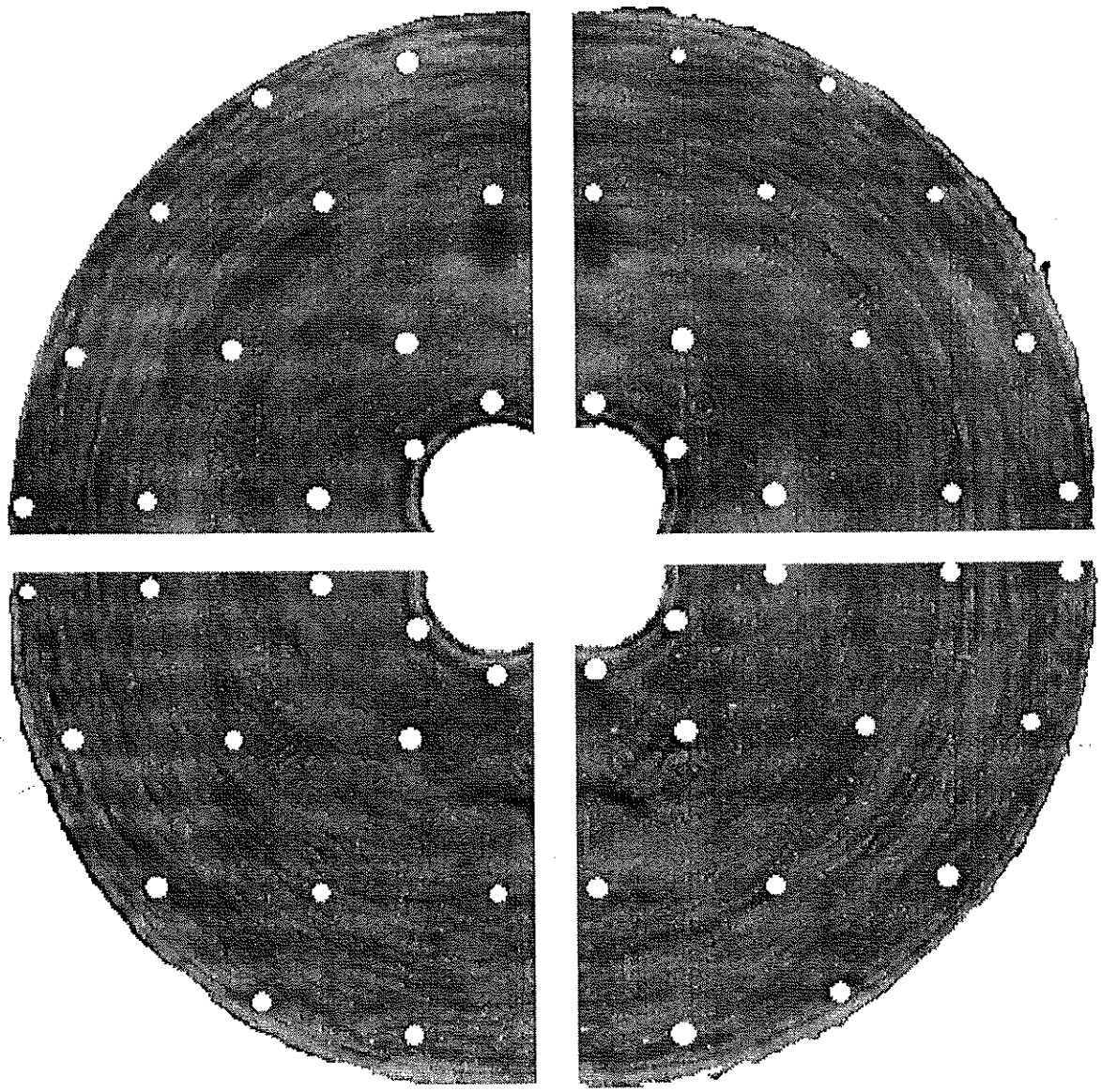

Figure 10. Gray-scale maps of 4 subapertures measured at twice the resolution of the full-aperture map. The gray scale covers ±100 nm of surface. The subaperture images are inverted left-right relative to the full-aperture images. The figures show the full measured wavefront and include some spurious pixels outside the polished surface. The fiducial markers were left on the mirror during the measurements, and their locations have been masked out of the images, as they were for the structure function calculation.

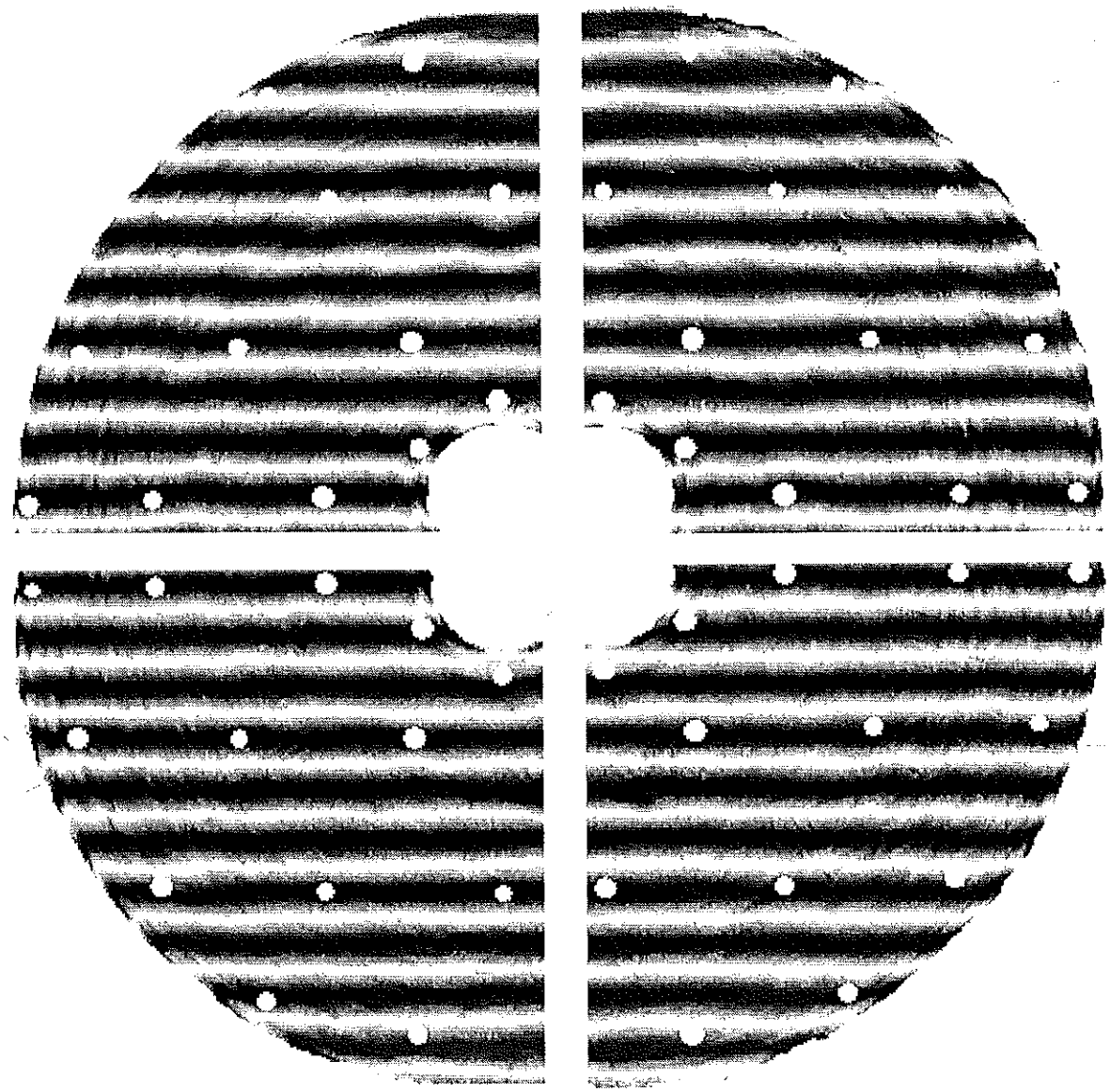

Figure 11. Synthetic interference patterns, calculated at 633 nm, for the 4 subapertures.

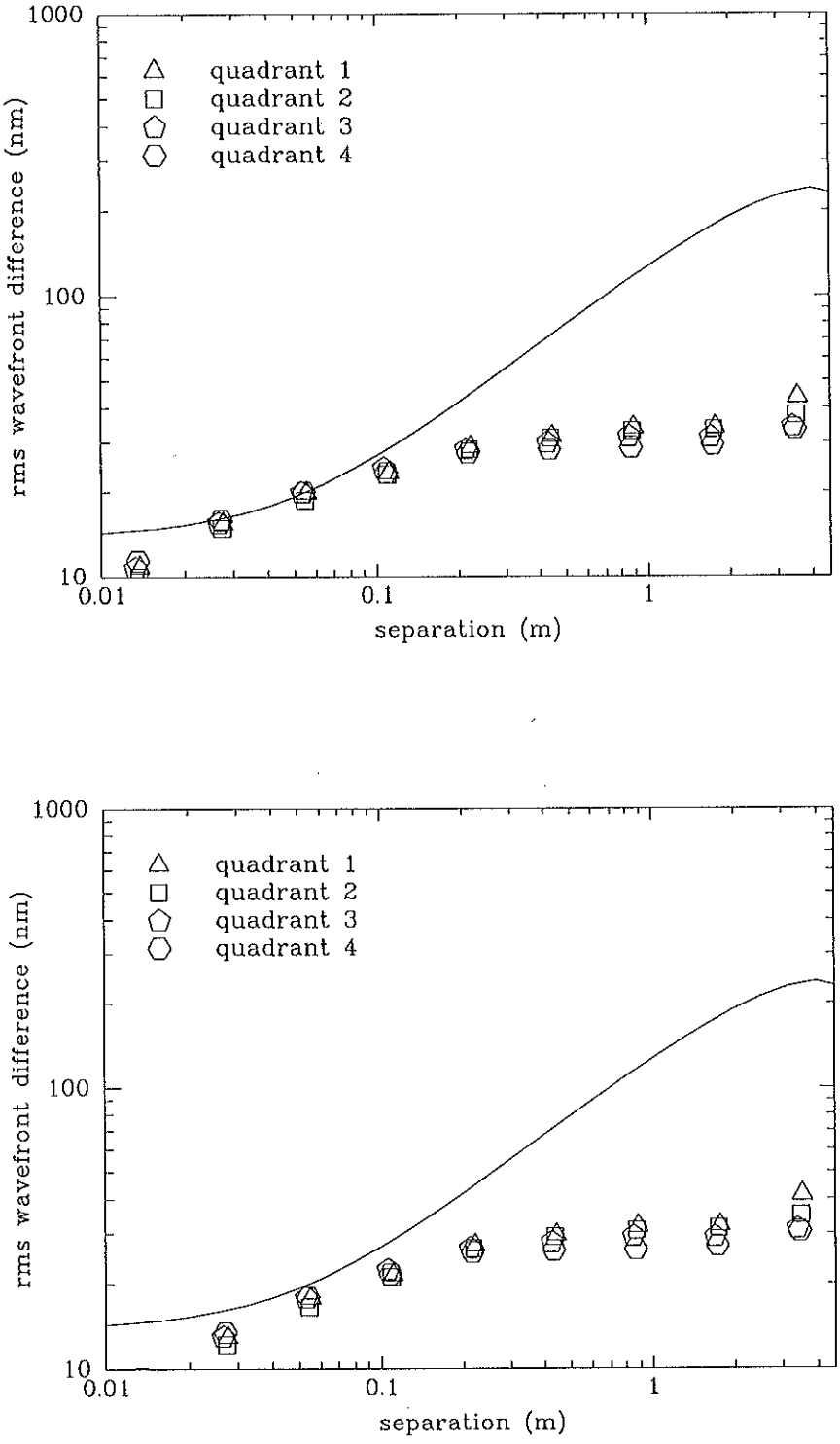

Figure 12. Square root of the wavefront structure function for the subaperture maps shown in Figure 10. Top: no correction for interferometer noise. Bottom: with structure function of interferometer noise subtracted. The curve is the specification.

6. Other measurements

6.1 Mechanical dimensions

We generated the mirror according to drawing 1168, Rev. C. Table 4 gives the finished dimensions, in inches to match the drawing. The inner and outer diameters, and bevel widths, match the drawing within the specified tolerances. The edge thickness given in drawing 1168, Rev. C fails to take account of the bevel. The correct value is 27.95 inches as listed in Table 4.

Table 4. Mechanical dimensions in inches

dimension	per drawing 1168, Rev. C	measured	uncertainty
front plate OD	256.40	256.43	0.01
back plate OD	256.40	256.44	0.01
front plate ID	35.00	34.98	0.005
back plate ID	37.00	36.97	0.005
polished surface OD	255.90	255.83	0.015
polished surface ID	35.50	35.51	0.01
edge thickness	27.950	27.970	0.005
wedge	0.0	0.015	0.002

The vertex thickness is calculated from the measured thickness and radius of curvature. Its value is 385.6 ± 0.1 mm, at the upper edge of the tolerance. The wedge angle is $12 \pm 2''$, well within the tolerance.

6.2 Faceplate thicknesses

We measured faceplate thicknesses with an ultrasonic gauge at 60 uniformly spaced cells. Table 5 gives the mean thickness, wedge, and radial variation for both faceplates. A positive radial variation means the outer edge is thicker. Both faceplates were measured after polishing was completed.

Table 5. Faceplate thicknesses in mm

	mean	wedge (p-v)	rotation angle of maximum	radial variation (p-v)
front plate	28.9	0.5	–162°	0.8
back plate	25.4	0.1	–73°	–0.6

6.3 Radius of curvature

We measured the vertex radius of curvature with a steel tape certified by NIST. The vertex radius of curvature is defined as the distance from the paraxial center of curvature to the vertex of the primary mirror. Since neither the vertex nor the center of curvature present a mechanical reference, we measure their separation indirectly by summing distances between intermediate surfaces.

The computer-generated hologram used to measure the null lens (see Section 7.3) is designed to return a null wavefront when it is placed at the paraxial center of curvature. We align the null lens at best focus of the primary mirror, as in the measurement of the primary mirror, and install the hologram mounted on a 5-axis stage. We adjust the stage to align the hologram to the null lens, thereby placing the hologram at the center of curvature. The lower reference is a two-ball locating jig that rests on the primary mirror surface near the edge of the center hole. We use the tape to measure from the 5-axis stage to the locating jig. The radius of curvature is the sum of this distance, the distance from the stage to the hologram, and the distance from the locating jig to the vertex, which is calculated from the approximate radius of curvature.

The final radius measurement was made on March 16, 2001. The result is

$$R = 16255.3 \pm 0.5\,\text{mm}. \tag{17}$$

6.4 Conic constant

The conic constant of the best-fit conic section is a sum of three terms:

1. spherical aberration in the final surface map;
2. correction for null lens error, based on the hologram;
3. correction for conic error caused by an error in radius of curvature.

The conic constant is sensitive to an error in the primary's radius of curvature because (a) the null lens and interferometer are positioned at best focus above the mirror, and (b) the test wavefront becomes more spherical as it propagates. The error in conic constant is related to the error in radius by

$$\frac{\Delta k}{k} = -\frac{\Delta R}{R}. \tag{18}$$

Table 6 gives the measured values and uncertainties for these terms. The uncertainty in the hologram correction is discussed in Section 7.3. From Table 6, the conic constant is

$$k = -1.00001 \pm 0.00008\,. \tag{19}$$

6.5 Centration of the optical axis

We determined the displacement of the optical axis relative to the mechanical axis (defined by the machined cylindrical surfaces at the outer edge of the mirror) by measuring the

Table 6. Measurement of conic constant

term	S (nm)	Δk (ppm)
uncorrected final map	-15 ± 10	-30 ± 20
hologram correction	35±40	70±70
radius correction	–25±15	–40±30
net error	–5±40	–10±80

change in coma when the mirror is rotated around its mechanical axis. If the optical and mechanical axes were coincident, rotating the mirror would introduce no coma. If they are not, rotating the mirror 180° changes coma by an amount equal to twice the coma corresponding to the displacement of the two axes.

We align the interferometer to the mirror at the standard rotation angle (0°) and measure the mirror, yielding coma coefficients $C_0|_0$ and $C_{90}|_0$. We then move the mirror to the turntable, rotate it 180°, and return it to the test tower. We monitor radial and vertical displacement with dial indicators to insure that the mechanical axis repeats within 0.1 mm. We tilt the mirror to obtain a tilt-free interference pattern, but do not translate it, and the interferometer is not moved. We then measure the mirror, yielding coma coefficients $C_0|_{180}$ and $C_{90}|_{180}$. Finally, we rotate the mirror back to 0° and repeat the first measurement; this result is averaged with the first, and their difference gives an indication of the uncertainty in the measurements. The coma that would be seen in the mirror, if the interferometer were aligned with the mechanical axis and the mirror at 0°, is half the difference of the coma measured at 0° and 180° rotations:

$$C_0|_m = \frac{C_0|_0 - C_0|_{180}}{2}, \tag{20}$$

$$C_{90}|_m = \frac{C_{90}|_0 - C_{90}|_{180}}{2}. \tag{21}$$

These coefficients are related to the displacement of the optical axis by[8]

$$C_0|_m = \frac{\Delta x}{384 f^3}, \tag{22}$$

$$C_{90}|_m = \frac{\Delta y}{384 f^3}, \tag{23}$$

where f is the focal ratio. A positive coefficient implies that the optical axis is displaced in the positive direction.

We made the final centration measurement on November 11, 2000. Further polishing after that date removed too little glass to affect centration significantly. Table 7 gives the measurements and inferred displacement of the optical axis. Values are given for the x and y components of coma and displacement, with uncertainty determined by repeating the procedure of rotating the mirror and measuring.

Table 7. Measurement of decenter coma

		value		uncertainty	
parameter	units	x	y	x	y
$C_0\|_0$, $C_{90}\|_0$	μm	0.01	–0.06	0.3	0.3
$C_0\|_{180}$, $C_{90}\|_{180}$	μm	0.06	–1.84	0.3	0.3
$C_0\|_m$, $C_{90}\|_m$	μm	–0.03	0.89	0.2	0.2
Δx, Δy	mm	–0.02	0.67	0.15	0.15
Δr	mm	0.67		0.15	
θ	degrees	92°			

6.6 Microroughness

We measured the microroughness at three locations on the mirror by making RTV replications and having them measured with a WYKO phase-shifting microscope interferometer. Five measurements were made at different positions on each 60 mm replication. The results are listed in Table 8. All results are under the specified roughness of 20 Angstroms. The average roughness is 9 Angstroms.

Table 8. Microroughness measurements

cell	radius (m)	average (Angstroms)	standard deviation (Angstroms)
D2	0.77	7.7	0.3
D8	1.92	9.1	0.3
D13	2.88	9.3	0.6
average		8.7	

6.7 Scratches, digs and bubbles

6.8 Internal flaws

Magellan 2 Final Inspection
Dean Ketelsen
14 June, 2001

On 12 and 13 June, Dennis Casper and myself performed the final inspection of the front surface of Magellan 2. While commonly referred to as a scratch-dig inspection, we were on the watch for defects of any kind remaining in the finished surface.

Method:
Dennis and I, after examining several features together so we were looking for the same thing, worked independently from foam pads, systematically searching the segments so no cores would be missed. On Magellan 1 a high-intensity lamp was used, the disadvantage being that the illuminated patch was very small, less than a cm diameter, making a flaw search very tedious and drawn out. As an alternative for this inspection, we used the DeWalt flashlights. They have very good intensity and rechargeable batteries and illuminated areas about 8cm diameter. Since the lower limit of scratch widths was 100 microns, during use with the flashlights we were easily able to find these and in fact find them down to about 25 microns in size. We are confident that we saw all scratches of 100 microns width or larger. While searching for digs is part of the specifications, the part had been polished out for some time and with the extended figuring involved in this mirror, no digs were visible on the surface.

Appearance:
The mirror surface is remarkably clean and free of defects. Likely due to the abovementioned length of rouge pitch polishing and figuring, there are few "new" defects - the scratches that are noted below might have been severe at one point, but are partially polished out, some parts of them disconnected lines of microscopic chips. All are less than the specified 200 micron maximum width and in fact, the longest is only 15 cm. On this mirror inspection, we were not looking for bubbles, but because of the large number exposed on the surface we had problems early on with crowsfeet. All exposed bubbles were treated by beveling with an abrasive stick to minimize these defects and in fact, only very tiny remnants of any crowsfeet exist in the final surface. While the large majority of bubbles had been cleaned of pitch and polishing compound after final polishing, the opticote process refills the bubbles, and it will likely need recleaning upon stripping after delivery.

Other Flaws:
While the spelled out search was for scratches and digs, we soon found defects not mentioned in the spec document. In these castings, seeds are commonplace in the faceplate area, and because of the local high stresses fractures are commonly seen near them. Several were found to be near or involved in the final polished surface. After some debate, it was decided to grind out the fracture area of only those whose fractures had reached the surface. Other seeds have fracturing, but are .5mm, 5mm or 10mm below the surface. Only those with fractures involved with the surface were treated.

Inspection Details:

Section A:

Core A2: Scratch near middle of core (double over portion of length).
100 micron X 7cm long.

Core A158: Seed w/fracture pattern near middle of core. 2.4mm diameter.

Section B:

Core B4: Scratch coming out of a bubble 100 microns X .6cm

Core B7: Seed with fracturing enters polished surface.~4mm diameter.

Core B38: Scratch coming out of a bubble 150 microns X .3cm.

Core B94: Scratch coming out of a bubble 150 microns X .2cm.

Section C:

Core C2: Scratch near center. Double scratch out of a bubble that where they widen join together. 150 microns X 3cm.

Core C81: Scratch near C93-C94 intersection. 100 microns X 6cm.

Core C136: Double scratch coming out of a bubble at widest 100 microns X 2 cm.

Section D:

Core D43: Seed/possible fracture near D58 rib. Fracture on upper part of seed, but may not extend to polished surface.

Core D84: Scratch near D70-D83 intersection. Max width 100 microns X7cm long. Some chipping, but partially polished out.

Core D143: Scratch near D142 rib. Widest 100 microns X7.5cm long.

Core D138: Seed/possible fracture near D139 rib. Mostly circular 1.5mm diameter. Fracture may not extend to surface.

Core D156: Seed/fracture near D148 rib. Associated with "brown" seed (inconel). Definate clamshell in surface .75mm diameter.

Section E:

Core E11: Scratch at E25-E26 intersection. 100 microns X 3cm long. Had chipping at one time, but partly - mostly polished out.

Core E52: Seed possible fracture towards E37 rib. Fracture may not extend to surface. 1.2mm diameter.

Core E78: Seed/fracture towards E65-E78 intersection. Seed is 1X4mm, fracturing mostly around upper end of seed.

Core E76: Scratch from bubble near center extending to E63 towards E62 rib. 100 microns widest, 15cm long. Some chipping, partially polished out.

Core E130: Seed/fracture near E140 rib. 1mm diameter, circular fractures

which may not extend to surface.

Core E113: Seed/possible fracture near E114 rib. May not extend to surface.

Core E152: Seed/possible fracture near E151 rib. Questionable whether it extends to surface.

Core E151: Seed/fracture near E150-E157 intersection. Extends to surface in 1.5mm diameter clamshell.

Bubble - largest bubble on Magellan 2 is on E170 near outboard rib. 9.5mm.

Section F:

Core F2: Scratch 100 microns X 2 cm.

Core F5: Scratch 150 microns X 2 cm.

Core F6: Seed/possible fracturing near F7 rib. 2.6mm diameter.

Core F31: Double scratch coming out of a bubble. 100 microns X 2cm.

Core F36: Scratch towards F50. 100 microns widest X 14cm. Double over part.

Core F37: Scratch out of a bubble. 100 microns X .2cm.

Core F58: Double scratch coming out of a bubble. 100 microns X 1cm.

Core F48: Scratch on a bubble towards F62, barely exceeding 100 microns X 20cm.

Core F89: Scratch coming out of a bubble. 100 microns X 1cm.

Core F89: Seed (cone shaped) near F77 rib. Possible fracturing.

Core F88: Seed with fracturing upwards towards surface bubble. Also scratch 100 microns X 12cm.

Core F114: Seed with small fractures (below surface). 2.5mm diameter.

Core F119: Seed near F129 rib. Possible fractures very close to surface.

Core F154: Large seed with fracturing, may not extend to surface.

Seed treatment:
After inspecting the 17 seeds noted, Randy Lutz treated 5 of them which had fractures extending to the surface. He used a battery powered Dremel with diamond tools to relieve the fracturing at the surface with water as a coolant. The treated seeds and their size at the surface:

Core B7: 3X4mm

Core D58-D43: 1.5mm

Core D156-D148: 1X2mm

Core E150-E151: 2mm

Core E78: 1X2mm

Scratch Area:
Taking the maximum width noted and the length of the scratch, total area is calculated to be 108.5 mm**2. This again is a maximum, as the scratch is typically much narrower on average than its maximum width noted. As it is, total scratch area of scratches over 100 microns in maximum width is just over a square cm.

STEWARD OBSERVATORY TECHNICAL DIVISION

MEMORANDUM

TO: **Matt Johns**

FROM: **Steve Warner**

RE: **Magellan 2 Scope of Work Compliance**

DATE: **June 22, 2001**

ATTACHMENTS: **B. Cuerden memo**

CC: **S. Miller, S. DeRigne**

The purpose of this memo is to demonstrate compliance with the "Scope of Work" document 96PR0114, Paragraph 4.1, deliverables, "A report with.....tests and measurements of the loadspreader and hardpoint attachments....". With this memo I have attached the specifications and test methods for lateral and shear proof testing of the loadspreader attachments called out by Brian Cuerden, Mechanical Engineer, Steward Observatory Technical Division and agreed upon by Dr. John Hill, Casting Director of Steward Observatory Mirror Lab.

Position

After the initial loadspreader bonding, a series of point-to-point measurements were made using 2 single-axis to triple loadspreader interfaces and a set of calibrated inside micrometers. Data was then sent to Brian Cuerden for analysis and with this analysis, several loadspreaders (#'s 101, 106 and 405) were shown to be out of tolerance. These were removed and re-bonded. Total RMS of the point-to-point measurements is reported as .006" with no point-to-point value over .020". A height gauge was then used to measure the loadspreader to glass dimensions at 4 points; the 3 static support lands and the center interface. This was a go/no-go system with .007" as the upper limit. All loadspreaders passed.

Proof Testing

Axial load testing was performed after the required cure time for the bonds. The procedure was to load test using a bar that spanned 3 triple loadspreaders, attaching a loadcell to the interface of the loadspreader in the middle. Jacking screws at either end of the bar were then torqued to give the appropriate load (950 lbs.) at the loadcell. The unit was left loaded for the prescribed period (1 minute) and the process repeated for all triple loadspreaders, with the exception of the 2 special triples. These have historically been ignored, as a failure would jeopardize the glass. All loadspreaders passed.

Lateral load testing was performed using a jig made up of 2 bars that attach to triple loadspreaders, a captivated belville washer stack and a turnbuckle. This system was calibrated on the puck pull-testing station and then used on the mirror. This unit was used for MMT, Magellan 1 and 2, and most recently, LBT 1. The specified load (450 lbs) was applied and left for the prescribed period (1 minute) and the process repeated for all triple loadspreaders. Singles, duals and the special triples were not tested, as a failure would jeopardize the glass. All loadpsreaders passed.

Hardpoint Wedge Bonding

The glass wedges were bonded to the mirror using Norland 61 Optical Adhesive. The wedges were scribed along the major axes during fabrication. The mirror was marked for these scribes during the layout procedure on the LOG. An autocollimator was mounted in the center of the mirror, the mirror was then leveled to 2 arc minutes and a zero point established using 2 sets of loadspreaders 180° apart. A thin (.003") layer of adhesive was applied and the wedge was aligned to the marks on the glass. The autocollimator was then used to set the proper angle of the wedge using a jig mounted with 2 optical flats installed onto the wedge and rotated to proper alignment with the autocollimator. UV light was then applied for the manufacturers specified time to bond the wedge in place. This process was repeated for all 6 glass wedges.

Results of Magellan 2 primary mirror integration

Steward Observatory Mirror Lab
June 26, 2001

1. Summary

We optimized the support forces for the second Magellan primary mirror in late May and early June, 2001. We chose to control 26 bending modes, and were able to do that with modest correction forces in the range $-31 < \Delta F < 23$ N. The resulting mirror figure is better than we obtained with the mirror on the polishing support. The rms surface error is 22 nm, reducing to 14 nm when astigmatism is subtracted. The image quality is also better than that on the polishing support, with 80% of the light at 500 nm contained in a 0.07″ diameter. Three sets of repeatability measurements demonstrated that this excellent image quality is maintained over several days.

2. Optimization of support forces

The mirror support system was installed in the cell and tested, the 6.5 m mirror was installed, and the system was made available for optical testing and force optimization beginning May 21, 2001. Initial results were limited by seeing (temperature gradients and turbulence in the air) that appeared worse than we had experienced while polishing the mirror. Temperature measurements revealed a thermal instability in the tower, the air handlers making the air at the top colder than the air in the main volume of the lab. The set point for the tower's air handler was adjusted on June 5, and this made a dramatic improvement in seeing. From this point, a single iteration of force adjustment gave the optimized figure presented here, obtained on June 6.

The optimization is done using the mirror's natural bending modes, calculated by BCV using finite-element analysis. Each orthogonal bending mode has a corresponding pattern of actuator forces. Working with Steve Shectman and Paul Schechter, we verified that the force patterns applied by the active support system produce the desired bending modes to high accuracy. We applied force patterns for 5 of the 20 softest modes, and mode 29. Results are given in Table 1 and Figure 1.

In all cases the amplitude of the desired mode is within 20% of the prediction, and within 8% for modes 1, 10, 12 and 13, which have better signal:noise. Leakage into astigmatism is as much as 22% in deflection for the modes with good signal:noise. When one takes into account the stiffness of the modes, this corresponds to less than 1% leakage in force. Even mode 29's 73% leakage in deflection corresponds to less than 0.5% leakage in force. There is negligible crosstalk between complementary modes (the pair of modes with even and odd symmetry about the y axis).

We used 26 modes for the final optimization. The correction forces are all in the range $-31 < \Delta F < 23$ N.

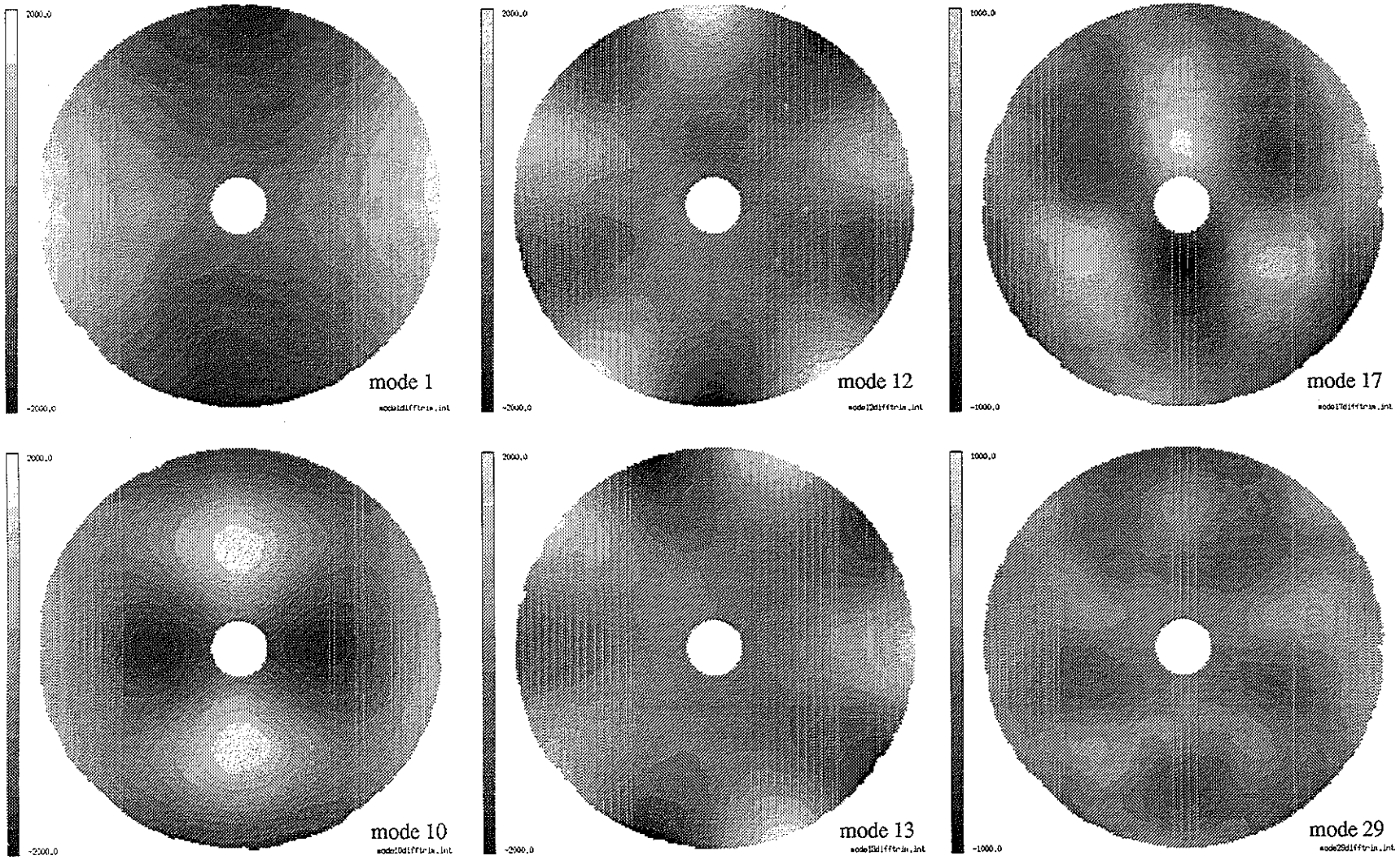

Figure 1. Measured bending modes obtained by applying calculated force sets. Gray-level bars are labelled in nm of wavefront (not surface). Modes 1, 10, 12 and 13 have similar signal:noise. Stiffer modes 17 and especially 29 have less signal but similar noise.

Table 1: Measured modal influence functions

mode	radial zero-crossings	azimuthal symmetry	rms force (N)	predicted rms deflection (nm)	measured rms deflection (nm)	rms in complementary mode (nm)	rms in astigmatism (nm)
1	0	2	2	336	349	11	
10	1	2	60	338	335	0	75
12	0	5	60	296	274	1	27
13	0	5	60	272	267	8	36
17	1	3	60	158	138	4	28
29	1	5	60	64	52	<6	47

3. Figure measurements

Figures 2 and 3 are surface maps and synthetic interference patterns from the measurements made with the optimized forces. All measurements have been corrected for errors in the null lens as determined by the hologram, and for image distortion as determined by the fiducials. A small amount of spherical aberration was subtracted (Zernike coefficient of 9 nm surface, corresponding to 17 parts per million in conic). While spherical aberration is well fit by the bending modes used, we chose not to correct it because the equilibrium value in the telescope will be determined by spacings. The interference patterns are calculated for a wavelength of 633 nm and contain 10 waves of tilt.

The rms surface error is 22 nm including astigmatism, and 14 nm after subtracting astigmatism. Results for the mirror on the polishing support were 150 nm including astigmatism (we made little effort to control it), 20 nm after subtracting astigmatism, and 16 nm after subtracting an additional 3 pairs of Zernike polynomials similar to flexible bending modes. The figure is significantly better on the active support with optimized forces. The figure error on the polishing support was dominated by a high-order astigmatism (mode 10, shown in Figure 1, and its complement) and a high-order spherical aberration. These aberrations were not present consistently over the last few measurements on the polishing support, and may have been due to temperature gradients. The high-order spherical aberration was not present when we optimized the support forces, and the high-order astigmatism, if it was present, was eliminated in the optimization.

4. Encircled energy

We calculated the encircled energy from the map shown in Figure 2. The diffraction calculation covers a 3.6 arcsecond field with 7.2 mas resolution, at a wavelength of 500 nm. Figure 4 shows encircled energy diagrams for the actual mirror and a perfect mirror, in perfect seeing and 0.25 arcsecond seeing. (Seeing is included by convolving the mirror's PSF with that of the atmosphere.) For comparison, Figure 5 shows the same quantities for the mirror on the passive polish-

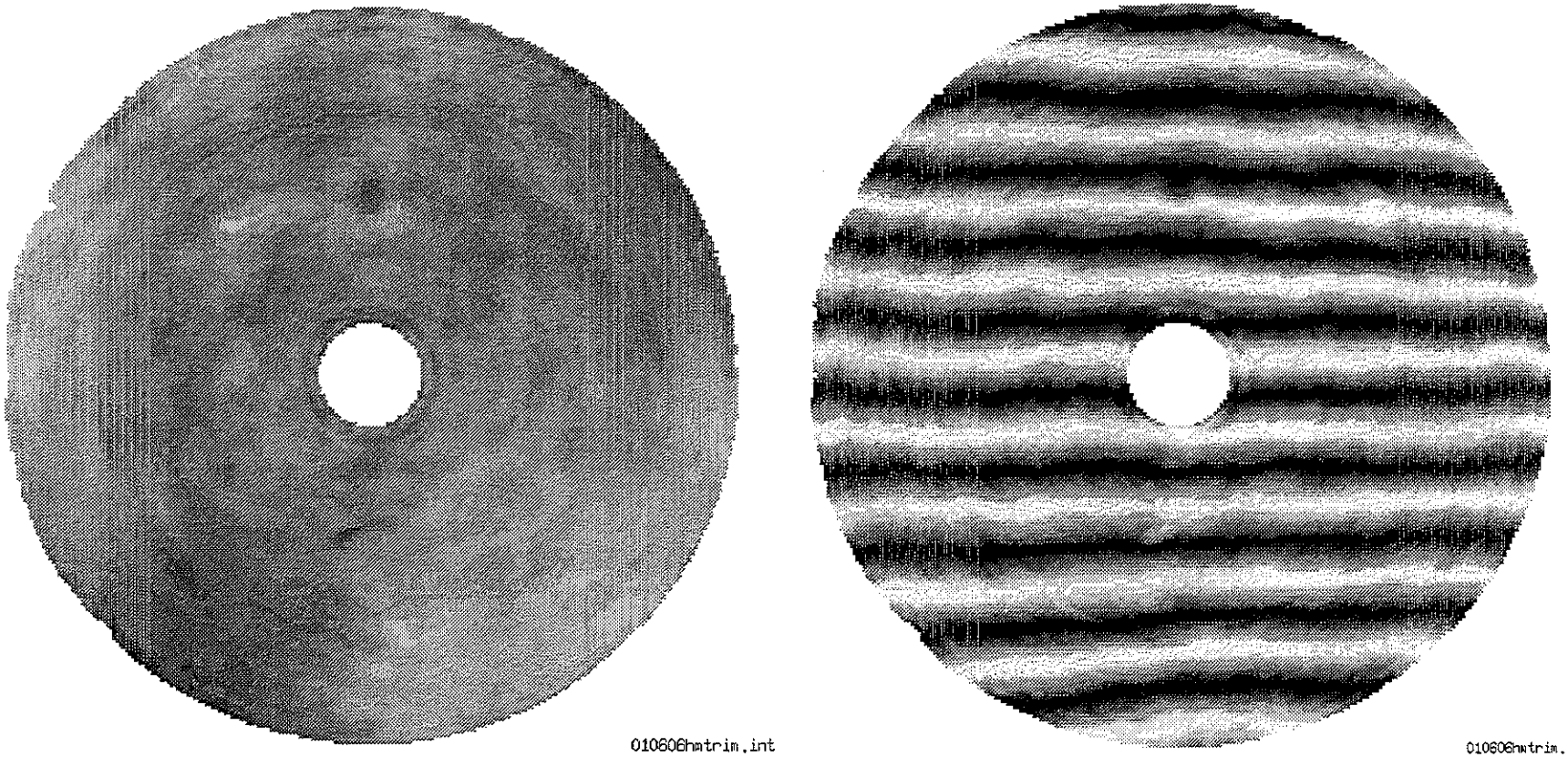

Figure 2. Gray-scale surface map and synthetic interference pattern for the optimized support forces. The gray scale covers ±100 nm of surface. The rms surface error is 22 nm.

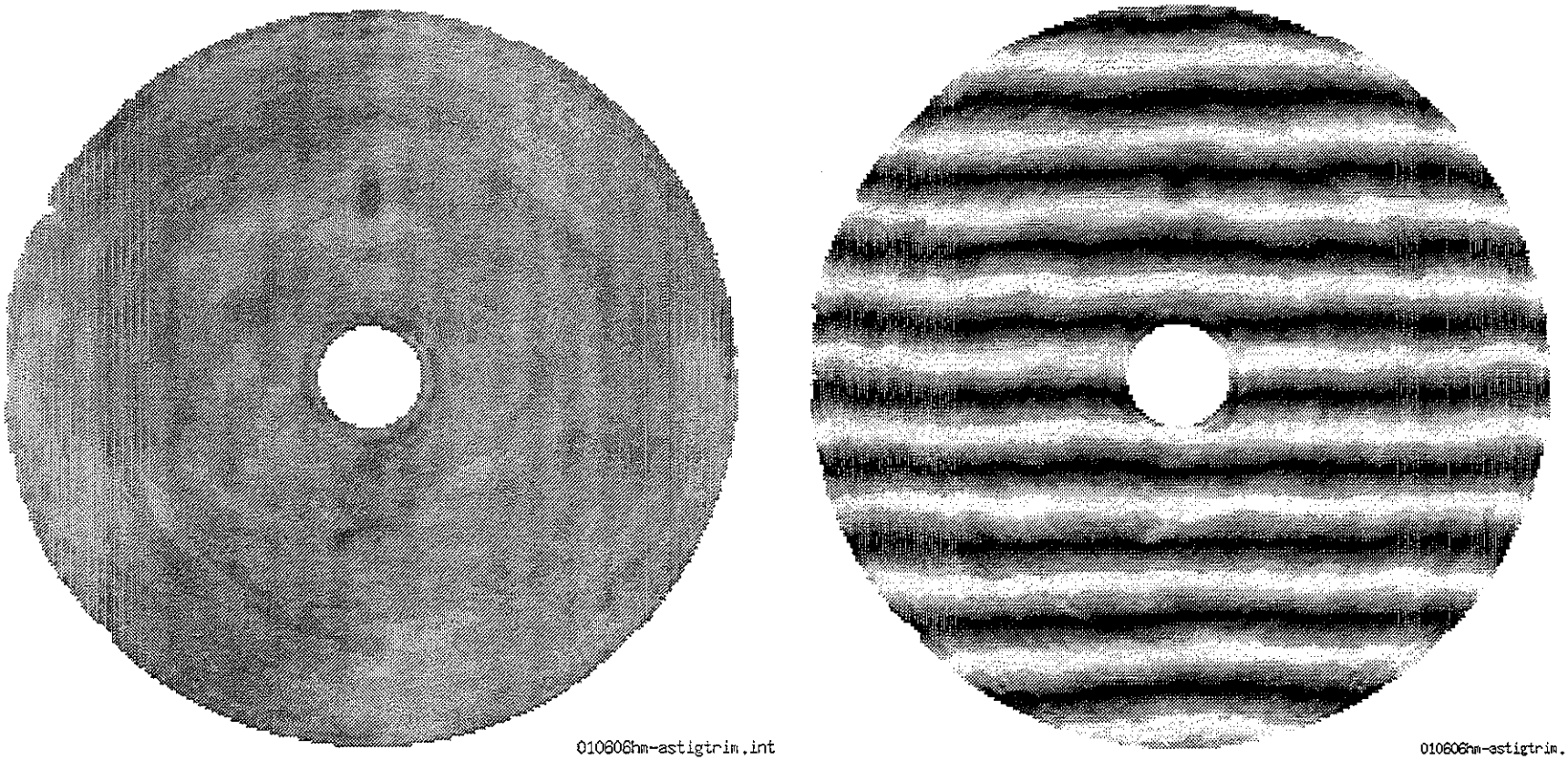

Figure 3. Gray-scale surface map and synthetic interference pattern for the optimized support forces, with astigmatism subtracted. The gray scale covers ±100 nm of surface. The rms surface error is 14 nm.

ing supports, after subtraction of astigmatism. Table 2 gives the diameter containing 80% of the energy for all cases. The mirror on optimized support forces performs better than the mirror on the polishing support.

Table 2: Image diameter containing 80% of the energy at 500 nm

	no seeing	0.25″ seeing
polishing support	0.08″	0.52″
telescope support	0.07″	0.52″
perfect mirror	0.04″	0.49″

5. Figure repeatability

We made three sets of measurements following the optimized results of June 6. In each case the forces were reoptimized, using successively fewer modes. The goal of this exercise was to see how well the lower modes such as astigmatism and trefoil could be controlled when we did not adjust the higher modes. As it turned out, we never improved on the June 6 results, although the final measurement on June 10 was slightly better on small scales and nearly as good on large scales.

Although we applied slightly different forces for the last three measurements, they illustrate the repeatability of the system. If it were perfectly repeatable, the small changes in force would have eliminated the residual astigmatism and other low bending modes obtained on June 6. The presence of these modes in the last three measurements represents non-repeatability, caused by variations in temperature gradients, support forces, or other factors. These measurements therefore give an upper limit on figure changes due to non-repeating forces.

Table 3 gives the surface error obtained in the final four measurements, starting with the best optimized figure of June 6. We also list the number of modes corrected in the current iteration, and the maximum force change in the current iteration. For the June 6 measurement, forces were optimized based on the previous measurement of June 5. For all later measurements, forces were optimized based on the June 6 measurement. (We always used the best measurement to date as the starting point for each iteration.) We give the rms surface error without any synthetic correction, and after subtracting several polynomials similar to the lowest bending modes.

Figure 6 contains encircled energy plots for the final four measurements, starting with June 6 (which is also shown in Figure 4). Table 4 gives the Strehl ratio (central intensity of the point-spread function relative to a perfect mirror) and the diameter θ_{80} containing 80% of the energy, both calculated at 500 nm. The encircled-energy diameters are nearly identical because the figure changes are on such large scales (primarily astigmatism and trefoil) that most of the light

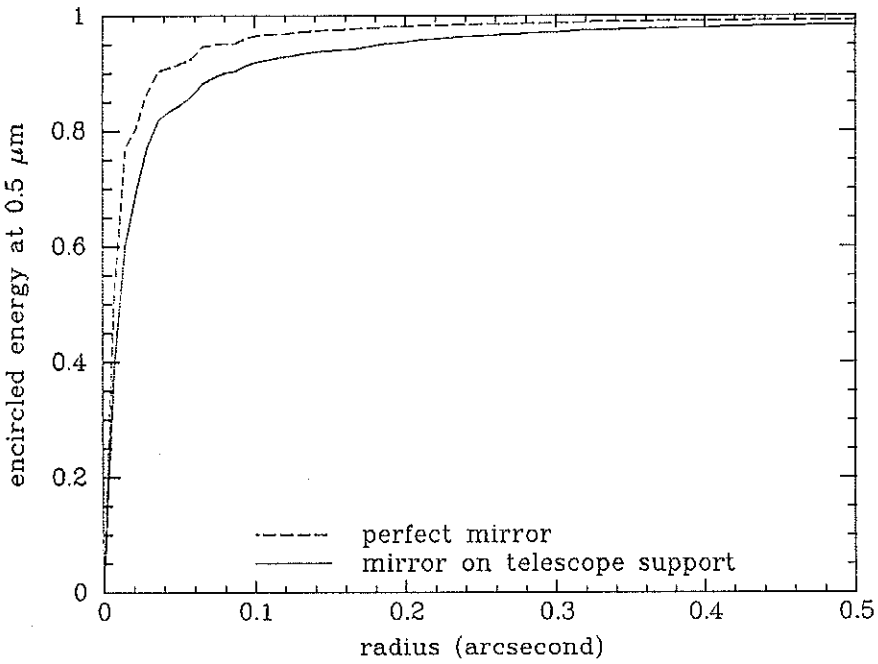

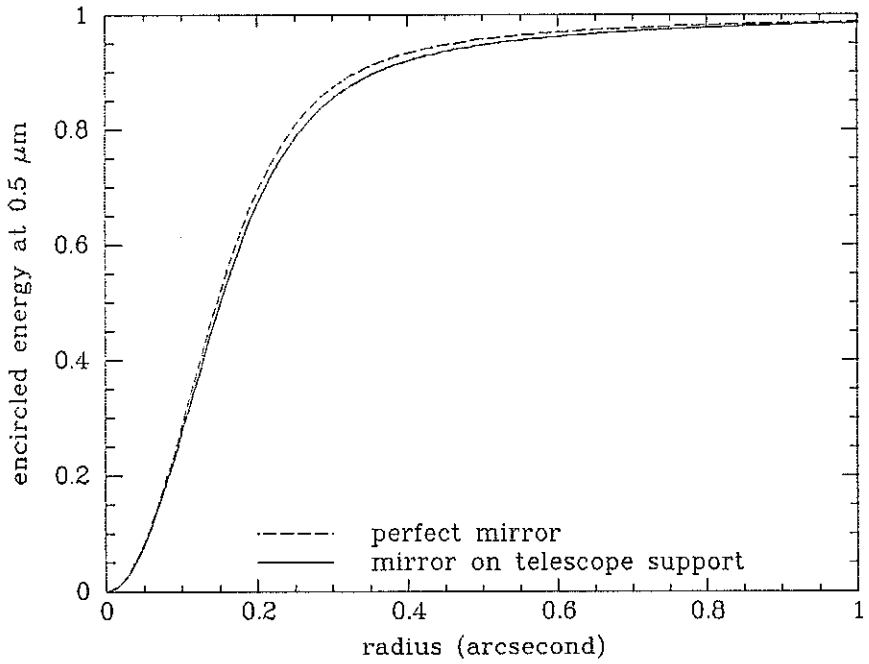

Figure 4. Encircled energy diagram for the mirror of Figure 2 and a perfect mirror. Top: in perfect seeing. Bottom: in 0.25 arcsecond (FWHM) seeing.

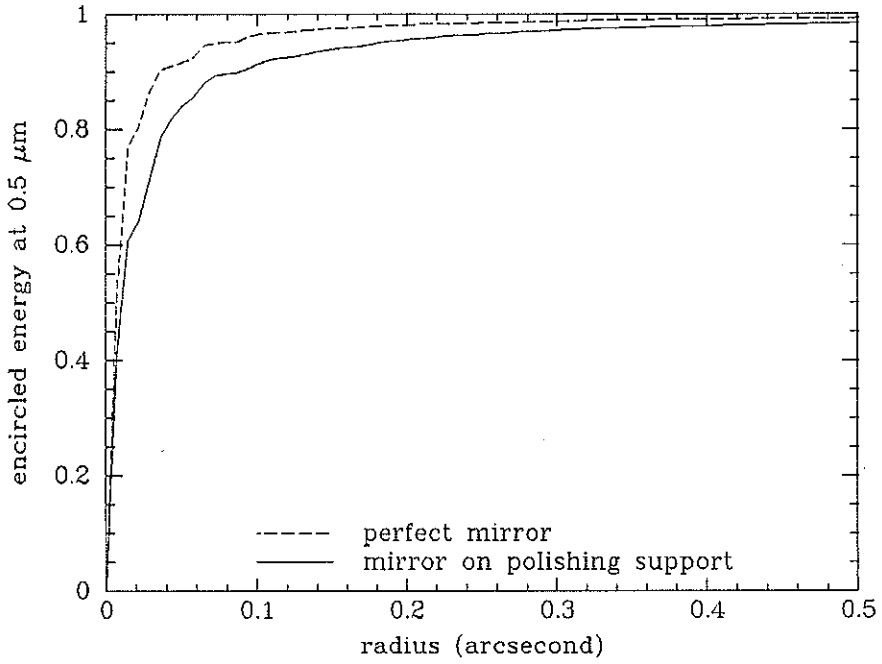

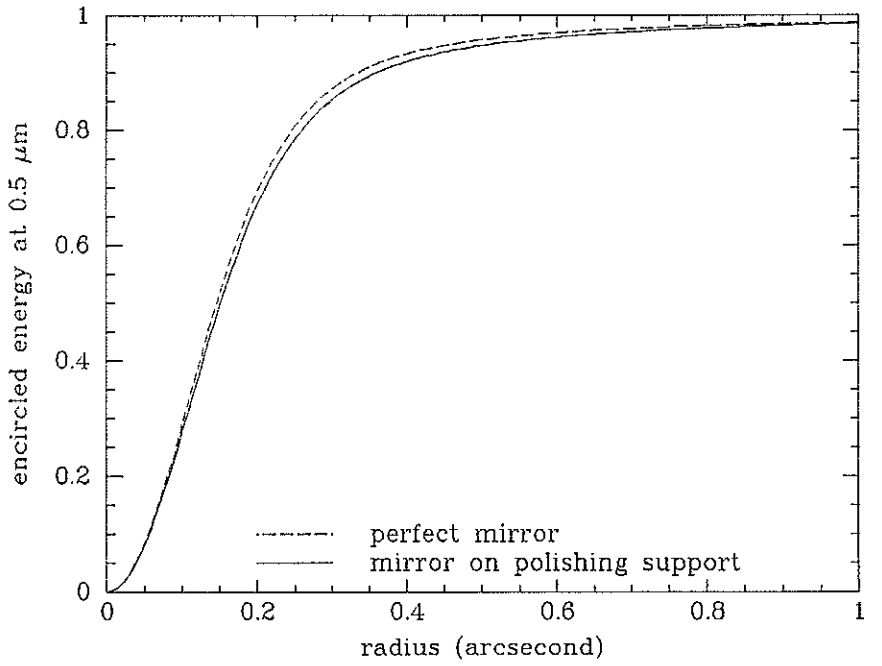

Figure 5. Encircled energy diagram for the mirror on the polishing support, with astigmatism subtracted, and a perfect mirror. Top: in perfect seeing. Bottom: in 0.25 arcsecond (FWHM) seeing.

Table 3: Figure repeatability

date	# modes corrected	max force change (N)	uncorrected rms surface error (nm)	astigmatism subtracted (nm)	+ trefoil subtracted (nm)	+ quatrefoil subtracted (nm)
June 6	26	13	22	14	13	12
June 7	20	6	26	15	15	13
June 8	14	5	28	24	16	16
June 10	9	2	24	16	15	13

remains inside a 0.07″ diameter circle. Thus there is very little degradation in image quality due to non-repeatability.

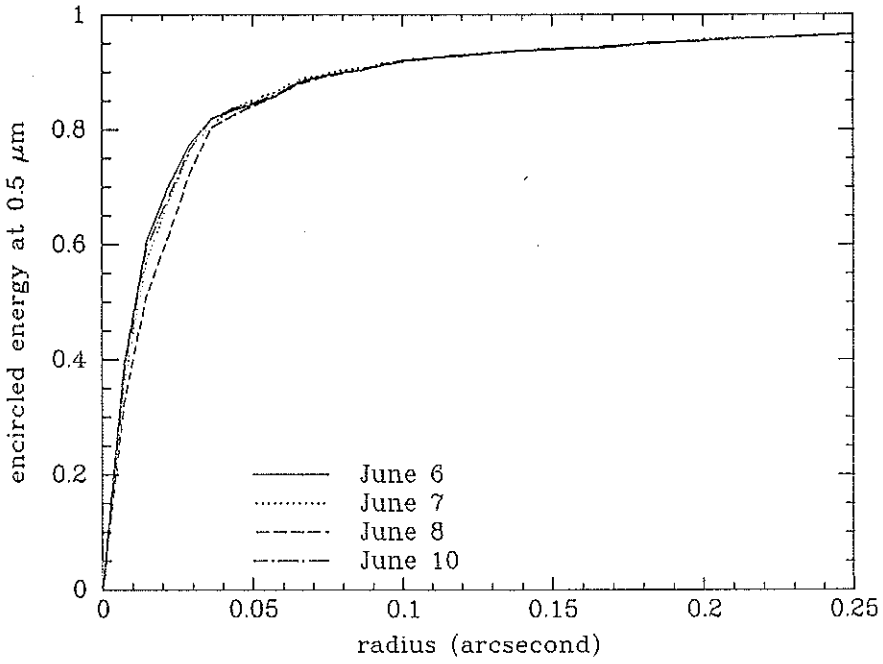

Figure 6. Encircled energy plots for the final four measurements, June 6-10.

6. Optimized forces

The optimized forces, used for the June 6 measurement, are listed in Table 5. These forces are added to the nominal forces from the BCV calculation. The optimized forces will also be transmitted electronically to Magellan staff.

Table 4: Image quality repeatability

date	Strehl ratio	θ_{80}
June 6	0.73	0.07″
June 7	0.64	0.07″
June 8	0.60	0.07″
June 10	0.70	0.07″

Table 5: Optimized forces

actuator ID	force (N)
1	10.4
2	19.9
3	11.8
4	10.2
5	14.1
6	-8.3
7	-1.4
8	3.6
9	0.5
10	-14.3
11	-9.3
12	-2.6
13	-6.0
14	-18.3
15	-14.1
16	-6.2
17	3.2
18	-3.2
19	-13.0
20	-1.8
21	9.1
22	5.0
23	-3.7
24	-3.8
25	16.3
26	7.0
27	-2.9
28	-0.1
29	11.4

Table 5: Optimized forces

actuator ID	force (N)
30	7.0
31	-7.3
32	-3.7
33	7.2
34	1.4
35	3.9
36	-8.7
37	-12.6
38	-0.4
39	3.5
40	-1.2
41	-13.2
42	-13.7
43	1.7
44	9.6
45	2.5
46	-11.9
47	7.6
48	17.7
49	-3.0
50	1.8
51	23.4
52	17.6
101	-2.2
102	1.7
103	6.5
104	-1.5
105	4.1
106	0.1
107	-1.6
108	7.5
109	9.9
110	-7.2
111	3.3
112	14.5
113	0.0
114	-25.3
115	-8.3
116	8.4
117	7.7

Table 5: Optimized forces

actuator ID	force (N)
118	-9.2
119	-17.7
120	-5.2
121	4.5
122	3.5
123	3.4
124	13.9
125	-7.3
126	1.3
127	7.8
128	15.5
129	-9.1
130	-5.4
131	-1.8
132	-3.2
133	3.7
134	-2.8
135	-2.1
136	-0.7
137	-15.2
138	-31.2
139	1.5
140	8.9
141	-0.6
142	-29.3
143	-2.7
144	4.0
145	13.6
146	-1.5
147	-9.7
148	3.5
149	10.4
150	-14.6
151	0.8
152	12.9